Gel nanostructure in alkali-activated binders based on slag and fly ash, and effects of accelerated carbonation

Susan A. Bernal[1,2*], John L. Provis[1,2*], Brant Walkley,[1] Rackel San Nicolas,[1]
John D. Gehman,[3] David G. Brice,[1,4] Adam R. Kilcullen,[1,4] Peter Duxson,[4]
Jannie S.J. van Deventer[1,4]

[1]Department of Chemical & Biomolecular Engineering, The University of Melbourne, Victoria 3010, Australia

[2] Department of Materials Science and Engineering, The University of Sheffield, Sheffield S1 3JD, United Kingdom

[3]School of Chemistry and Bio21 Institute, The University of Melbourne, Victoria 3010, Australia

[4]Zeobond Pty Ltd, P.O. Box 23450, Docklands, Victoria 8012, Australia

* To whom correspondence should be addressed. Email j.provis@sheffield.ac.uk, s.bernal@sheffield.ac.uk phone +44 114 222 5490, fax +44 114 222 5493

Abstract

Binders formed through alkali-activation of slags and fly ashes, including 'fly ash geopolymers', provide appealing properties as binders for low-emissions concrete production. However, the changes in pH and pore solution chemistry induced during accelerated carbonation testing provide unrealistically low predictions of in-service carbonation resistance. The aluminosilicate gel remaining in an alkali-activated slag system after accelerated

carbonation is highly polymerised, consistent with a decalcification mechanism, while fly ash-based binders mainly carbonate through precipitation of alkali salts (bicarbonates at elevated CO_2 concentrations, or carbonates under natural exposure) from the pore solution, with little change in the binder gel identifiable by nuclear magnetic resonance spectroscopy. In activated fly ash/slag blends, two distinct gels (C-A-S-H and N-A-S-H) are formed; under accelerated carbonation, the N-A-S-H gel behaves comparably to fly ash-based systems, while the C-A-S-H gel is decalcified similarly to alkali-activated slag. This provides new scope for durability optimisation, and for developing appropriate testing methodologies.

Keywords: alkali-activated cements; slag; fly ash; carbonation; NMR spectroscopy.

1. Introduction

The development and assessment of alkali-activated materials has become increasingly widespread over the past 60 years, motivated by the environmental and technological advantages that these materials can exhibit, compared with conventional Portland cement systems [1]. However, in spite of the in-service performance that has been displayed during this time in various applications, particularly in Ukraine, Russia and China [1], there is still some uncertainty regarding the long-term durability of these materials. This is the primary issue that needs to be addressed to build the acceptance and confidence required for the use of these alternative materials in industrial scale applications [2, 3].

In testing the durability of alkali-activated binders, the methods applied to conventional Portland cements are usually adopted, often without questioning the relevance or physical

meaning of the information collected from those tests. This is particularly the case for accelerated carbonation test methods, where the comparability between different experimental studies is low due to the lack of a widely accepted standardised test procedure; a European standard test method for the assessment of carbonation of conventional cements has been developed [4], and the validation of this method for alternative cements has not yet been undertaken. This means that the studies reported in the literature have been conducted under a wide range of different environmental exposure conditions. Additionally, the environmental chambers used to induce accelerated carbonation cannot replicate the variations in temperature, humidity, wet-dry cycling, and other conditions to which the concretes can be exposed during 'real life' service [5].

The European standard EN 13295 [4] claims that under the carbonation testing conditions proposed (1% CO_2, 21 ± 2ºC, relative humidity 60 ± 10%), the carbonation products formed are similar to those identified in naturally carbonated specimens. On the other hand, there is no specific standard or recommendation for the assessment of carbonation of alkali-activated binders, and the few studies specifically examining the carbonation of these materials [6-9] have been conducted using different exposure conditions, with CO_2 concentrations ranging between 1 - 100%. This has led to conflicting conclusions about the actual resistance of alkali-activated binders to carbonation, the mechanism by which the carbonation reaction proceeds in these systems, and whether these mechanisms can be interpreted in the same way as in Portland cement systems.

A particular complication in the case of alkali-activated binders is the apparent divergence between the performance observed under accelerated carbonation conditions, and the observations of the performance of existing aged structures in service. Shi et al. [1] report

natural carbonation rates for alkali silicate-activated slag concretes lower than 1 mm/year, while laboratory studies have shown carbonation depths in alkali-activated concretes between 13 mm to 25 mm after 240 h of exposure to 7% CO_2 [10]. As a point of comparison, Ho and Lewis [11] report that for Portland cement concretes, 1 week (168 h) of exposure to 4% CO_2 is approximately equivalent to 1 year of natural carbonation. This means that the accelerated carbonation test appears almost an order of magnitude more aggressive towards alkali-activated concretes compared to Portland cement concretes.

A study of carbonation rates in alkali-activated slag/metakaolin concretes [12] also showed that the progress of carbonation is strongly dependent on the CO_2 concentration used during accelerated testing, due largely to differences in the total porosity and capillary pore structure induced at higher CO_2 concentrations. Recent studies of carbonation of alkali-activated slag binders [12, 13], including thermodynamic simulations of the carbonation of highly alkaline pore solutions [13], have demonstrated that carbonation of Ca-rich activated binders is likely to occur in two stages. The first step is the carbonation of the pore solution by absorption of CO_2 from the atmosphere, leading to a reduction in pH and the eventual precipitation of Na-rich carbonates. The second step then involves the reaction of the dissolved carbonates with the solid binder, with partial decalcification of Ca-rich binder phases leading to the formation of Ca-rich carbonates. However, questions remain regarding the likelihood of this second step taking place in alkali-activated fly ash binders, as the key gel phases are not Ca-based.

The chemistry and structural development of alkali-activated fly ash is quite different from that of alkali-activated slag or conventional Portland cement-based binders, which is associated with the differences in the levels of calcium in these binders [14, 15]. There is little existing understanding of the effect of CO_2 exposure on the durability of these materials, although

carbonation due to absorption of CO_2 from the atmosphere has been identified as being potentially significant in binders with high pore solution alkali concentrations. Criado et al. [16], in assessing the effect of different curing conditions of alkali-activated fly ash, identified sodium-containing crystalline products of pore solution carbonation during open curing. The specimens with carbonated pore solutions also revealed a lower extent of reaction and lower mechanical strengths compared with uncarbonated binders cured at moderately elevated temperatures (85ºC). This is likely to be partially associated with the consumption of the alkalis during the carbonation reaction, inducing a reduction in the solution pH, and consequently a decreased extent of reaction of the fly ash. Bijen and Waltje [17] identified an acceleration in carbonation of NaOH-activated slag/fly ash binders due to intensive microcracking of their specimens during drying prior to CO_2 exposure.

Therefore, there is a need for detailed assessment of the effects of CO_2 exposure on the structure of these binders, and such discussion is presented in this paper, via the application of X-ray diffraction, thermogravimetry, ^{29}Si and ^{27}Al MAS NMR spectroscopy, and scanning electron microscopy. The effects of exposing alkali-activated binders based on slag, fly ash, and their blends, to different CO_2 concentrations are analysed in terms of chemical and microstructural changes in the binder, and the formation of distinct carbonation products depending on binder chemistry and exposure conditions.

2. Experimental program

The aluminosilicate precursors used in this investigation were a fly ash (FA), ASTM Class F, from Bayswater Power Station, New South Wales, Australia, and a granulated blast furnace slag (GBFS) supplied by Zeobond Pty Ltd, Australia. The oxide compositions of the precursors

are given in Table 1. Detailed quantitative mineralogical characterisation of Bayswater fly ash has recently been published by Williams and Van Riessen [18], who found 59% amorphous content, with identifiable crystal phases quartz (16%), mullite (21%), and minor iron oxides.

Table 1. Compositions of the FA and GBFS used. LOI is loss on ignition at 1000°C

Component (mass % as oxide)	FA	GBFS
SiO_2	62.9	33.8
Al_2O_3	24.9	13.7
Fe_2O_3	5.2	0.4
CaO	<0.1	42.6
MgO	1.0	5.3
Na_2O	0.2	<0.1
K_2O	1.3	0.4
Others	1.8	3.7
LOI	2.7	1.8

The alkali activator was prepared by dissolution of solid NaOH pellets (Sigma-Aldrich, Australia) into D grade (PQ, Australia) sodium silicate, to reach a solution modulus (Ms = SiO_2/Na_2O) of 1.0. The Na_2O dose supplied by the activator was 4.0 g per 100g solid precursor (slag + fly ash). Water was added to the activating solution to reach a water/binder ratio of 0.40, and the activator was allowed to cool to room temperature prior to preparation of the specimens. Pastes were produced based on alkali-activated slag, fly ash, and a 1:1 blend of the two precursors, and cured in sealed bags at 23°C.

2.1 Accelerated carbonation

After 1 and 7 days of curing, samples were crushed to pass a 74 μm sieve, and placed in a humidity-controlled, CO_2-controlled testing chamber to induce accelerated carbonation. The curing and exposure regimes were selected to replicate in part the industrial application of

premixed concretes, where the concretes are exposed to the atmosphere (and thus prone to carbonation) in the first few weeks of service, and the samples were crushed to give rapid carbonation under the test conditions. The accelerated carbonation tests were conducted at CO_2 concentrations of 1.0, 3.0 and 5.0 % (controlled to within ±0.2 % in each case), a temperature of 23±2°C, and relative humidity (RH) 65±5 %. Specimens were removed from the chamber after 1 and 7 days of exposure. Properties of samples that were not exposed to CO_2, and instead were kept sealed until reaching similar ages to the carbonated specimens after exposure and then crushed and analysed immediately, are used as references. Samples were analysed by:

- X-ray diffraction (XRD), using a Bruker D8 Advance instrument with Cu Kα radiation, a nickel filter, a step size of 0.020º, and a 2θ range of 3 - 70º.
- Solid-state ^{29}Si MAS NMR spectra were collected at 119.1 MHz on a Varian INOVA-600 (14.1 T) spectrometer using a probe for 4 mm o.d. zirconia rotors and a spinning speed of 10.0 kHz. The ^{29}Si MAS experiments employed a pulse width of 6 µs, a relaxation delay of 20 s and 4300-6500 scans. Solid-state ^{27}Al MAS NMR spectra were acquired at 156.3 MHz on the same instrument, with a pulse width of 6 µs, a relaxation delay of 2 s, and a minimum of 1000 scans. All spectra were collected with a pulse angle of 51º. ^{29}Si and ^{27}Al chemical shifts are referenced to external samples of tetramethylsilane (TMS) and a 1.0 M aqueous solution of $AlCl_3 \cdot 6H_2O$, respectively.
- Thermogravimetry was carried out using a Perkin Elmer Diamond instrument, using a heating rate of 5ºC/min between 40ºC and 700ºC, and 10ºC/min between 700ºC and 1000ºC, with a nitrogen purge at 200 mL/min. To provide consistency in the initial states of all samples analysed, samples were held in the instrument (powdered samples of ~100 µg in an alumina crucible) at 40°C for 60 minutes prior to the start of heating.

- Environmental scanning electron microscopy (ESEM) was conducted using an FEI Quanta instrument with a 15 kV accelerating voltage and a working distance of 10 mm. To avoid the need to carbon-coat the samples, polished samples were evaluated in low vacuum mode using a backscatter detector. A Link-Isis (Oxford Instruments) X-ray energy dispersive (EDX) detector was used to determine chemical compositions.

3. Results and discussion

3.1. X-ray diffraction

3.1.1 Uncarbonated samples

X-ray diffraction data collected from alkali-activated slag paste samples at 8 and 14 days of age, and from the interior region of the specimen after 3 years of exposure to air, are presented in Figure 1. Some of these data have previously been briefly reported in the context of a discussion of pore solution chemistry [13], and are used here to demonstrate the structural changes induced in the binder gel by accelerated carbonation.

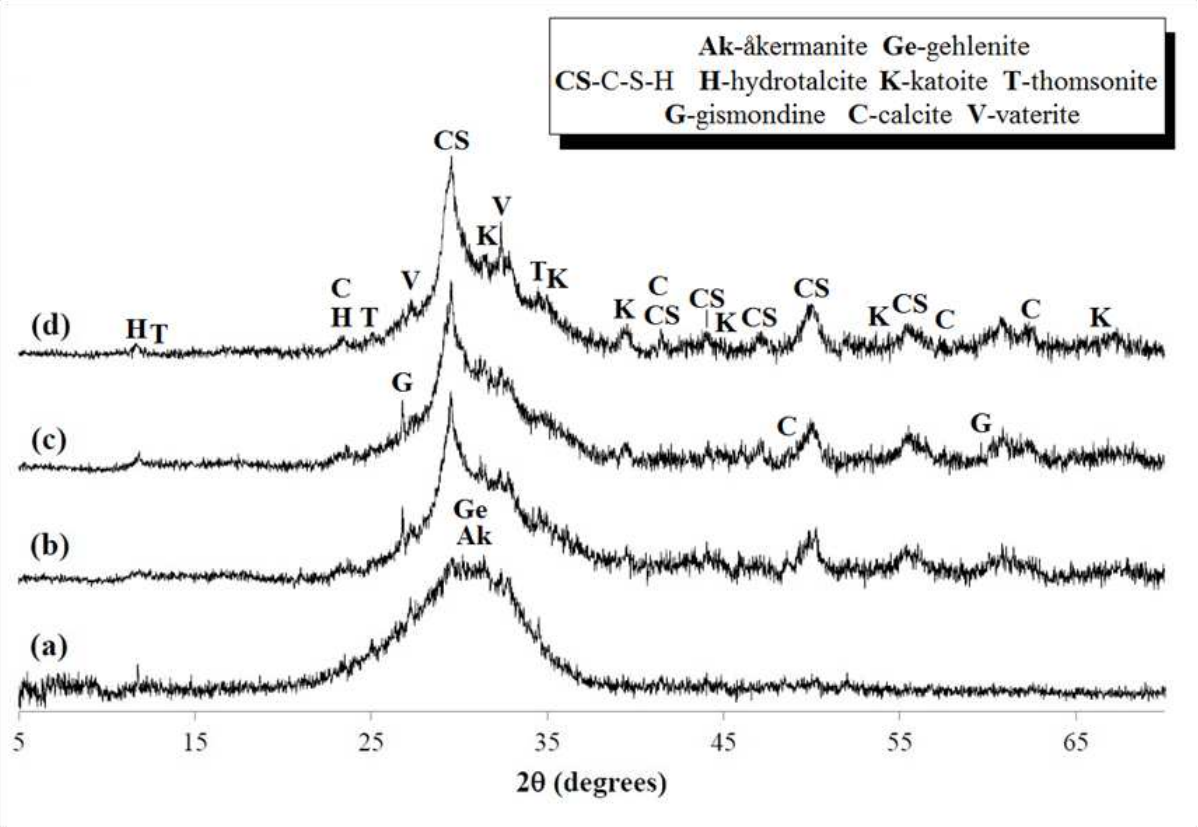

Figure 1. X-ray diffractograms of (a) unreacted slag, and unexposed alkali-activated slag after (b) 8 days, (c) 14 days, and (d) 3 years of curing

Small amounts of åkermanite and gehlenite are identified in all binders, as remnant crystalline phases of incompletely reacted slag particles. The main reaction product, a poorly crystalline calcium silicate hydrate (C-S-H), provides only weak Bragg reflections but shows some structural similarities to tobermorite ($Ca_5(Si_6O_{16})(OH_2)$, PDF# 01-089-6458). Hydrotalcite ($Mg_6Al_2(CO_3)(OH)_{16}{\cdot}4H_2O$, PDF# 00-041-1428) is also observed as a reaction product, which is consistent with other studies of alkali-activation of slags containing åkermanite [19-22]. A zeolitic product with a gismondine type structure is identified in samples after 14 days of curing, while thomsonite is observed in aged activated slag pastes. The formation of these zeolites in alkali-activated binders is consistent with reports in the literature, and is discussed in detail elsewhere [13].

In the 3-year cured samples, a small amount of katoite (siliceous hydrogarnet, $Ca_3Al_2(SiO_4)_{3-x}(OH)_{4x}$ with $1.5 \leq x \leq 3.0$, PDF #00-038-0368) is also observed. The identification of katoite in aged Na_2SiO_3-activated slags suggests that the relatively high content of Si here leads to the formation of katoite instead of (or potentially in addition to) AFm phases. Any AFm regions present are not directly identifiable by XRD, but this point will be revisited in section 3.3 in the context of the discussion of NMR spectra. The formation of structural motifs similar to those of AFm phases has previously been indicated in hydroxide-activated slags, where it was proposed that some of the aluminium exists in AFm-like layers, intimately intermixed into the C-S-H structure and thus not distinguishable by XRD [21, 23].

Figure 2 shows X-ray diffractograms of the unreacted fly ash, with unreacted crystal phases quartz (PDF# 00-046-1045), mullite (PDF# 01-083-1881), and iron oxides, probably with some degree of substitution of various divalent and trivalent cations, and structurally similar to maghemite (PDF# 00-039-1346) and hematite (PDF#01-085-0599). The crystallographic differences between the unreacted fly ash and the as-cured specimens are only minor. There is a slight shift in the broad feature due to disordered aluminosilicates, which moves from a position centred around 23° 2θ due to the glasses in fly ash, to a slightly higher angle in the aluminosilicate binder gel [24], but there is no evidence of formation of crystalline reaction products, and the crystalline components of the ash appear unreactive.

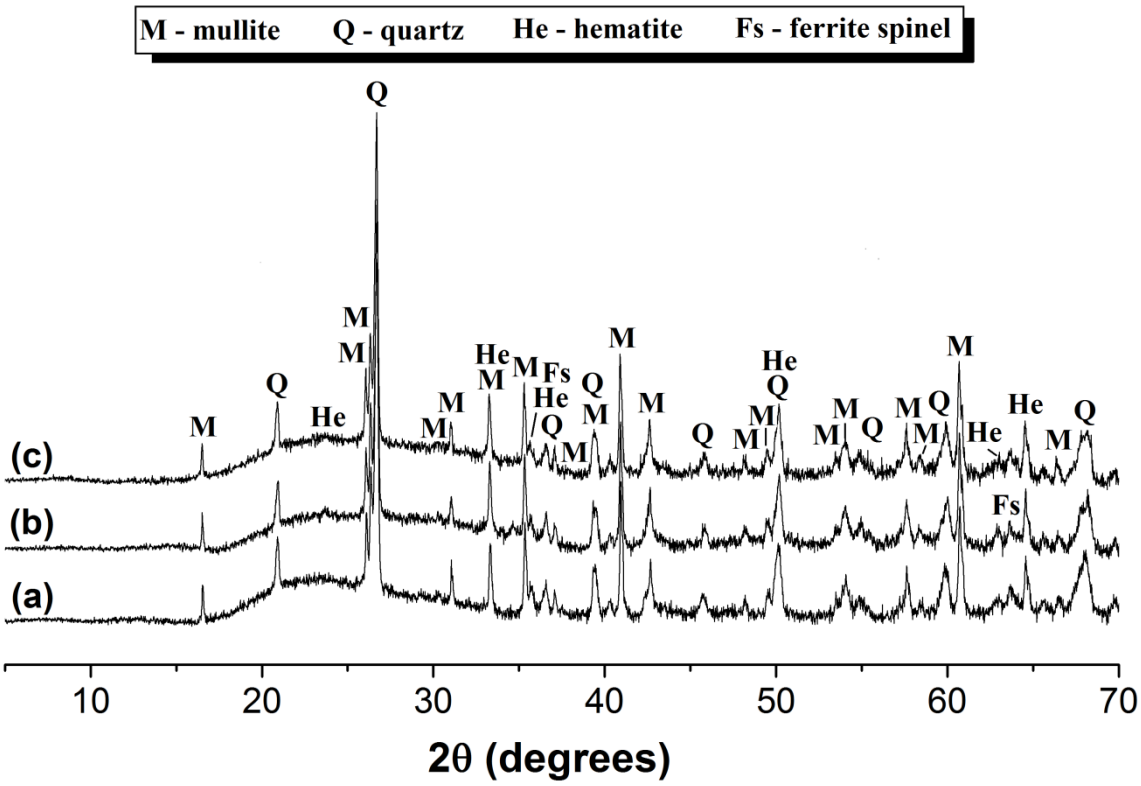

Figure 2. X-ray diffractograms of (a) unreacted fly ash, and uncarbonated samples after (b) 8 and (c) 14 days of curing.

Figure 3 presents X-ray diffractograms of the as-cured alkali-activated binder samples based on a 1:1 blend of fly ash and ground granulated blast furnace slag, with diffractograms of the raw fly ash and slag for comparison purposes. The quartz, mullite and iron oxides from the fly ash are evident in the reaction products, as in Figure 2, and the broad feature due to the presence of silicate and aluminosilicate gel phases is again visible between 25-35° 2θ. The provision of additional curing time gives additional crystallinity in the C-S-H type gel (which almost certainly has a significant degree of Al substitution). There is some variability in mullite and quartz peak intensities between the two as-cured samples, but this is attributed to variability within the larger fly ash particles present in each of the XRD specimens, rather than indicating chemical reaction processes.

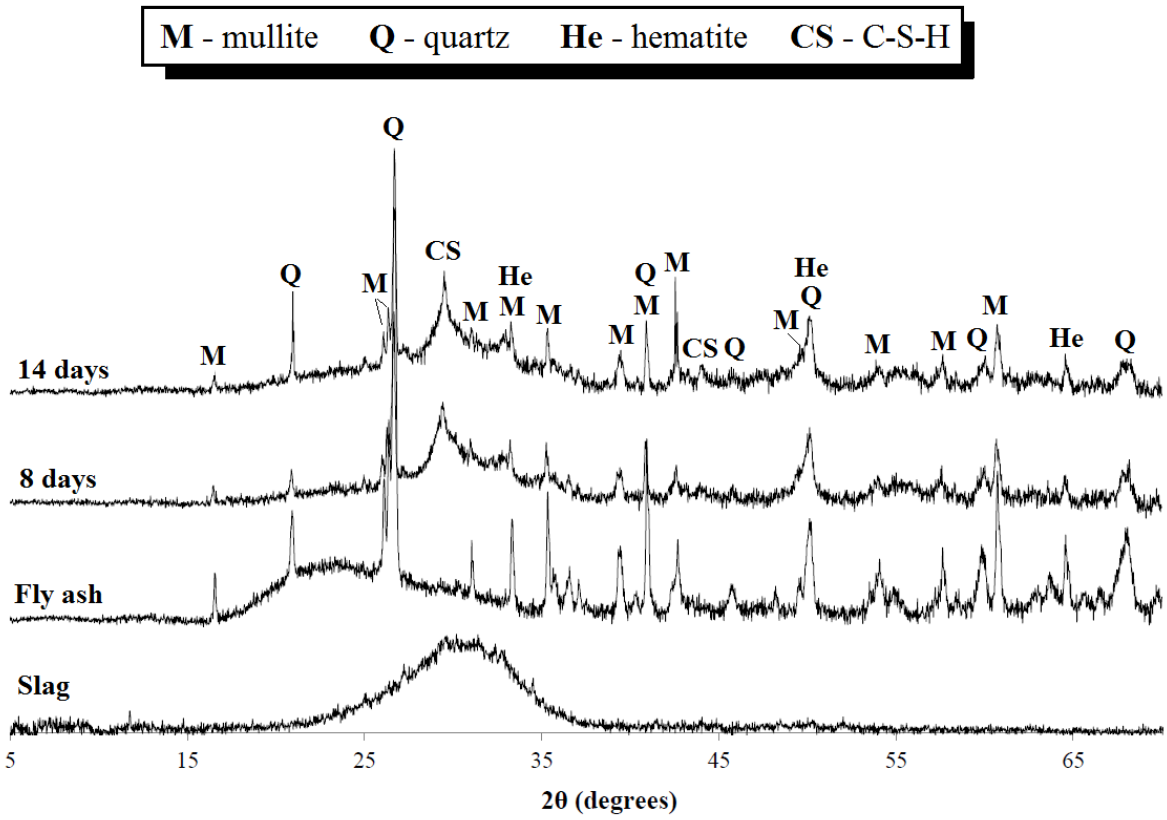

230

231 **Figure 3.** X-ray diffractograms of unreacted slag and fly ash, and alkali-activated fly ash/slag
232 blends cured for 8 or 14 days.

233

234 3.1.2 Carbonated specimens

235 Three different polymorphs of calcium carbonate: calcite (PDF# 01-083-0577), vaterite (PDF#
236 01-074-1867) and aragonite (PDF# 00-003-1067), are evident in the XRD results for
237 accelerated carbonated alkali-activated slag specimens, cured for 1 day (Figure 4A) and 7 days
238 (Figure 4B) and subsequently carbonated for 7 days. These are the main crystalline carbonation
239 products. Vaterite is the predominant product resulting from exposure of the material to
240 elevated CO_2 levels, increasing with curing time and CO_2 concentration. Conversely, the peaks
241 corresponding to calcite are more intense in samples carbonated at lower CO_2 concentrations,
242 especially in specimens exposed to CO_2 after 1 day of curing.

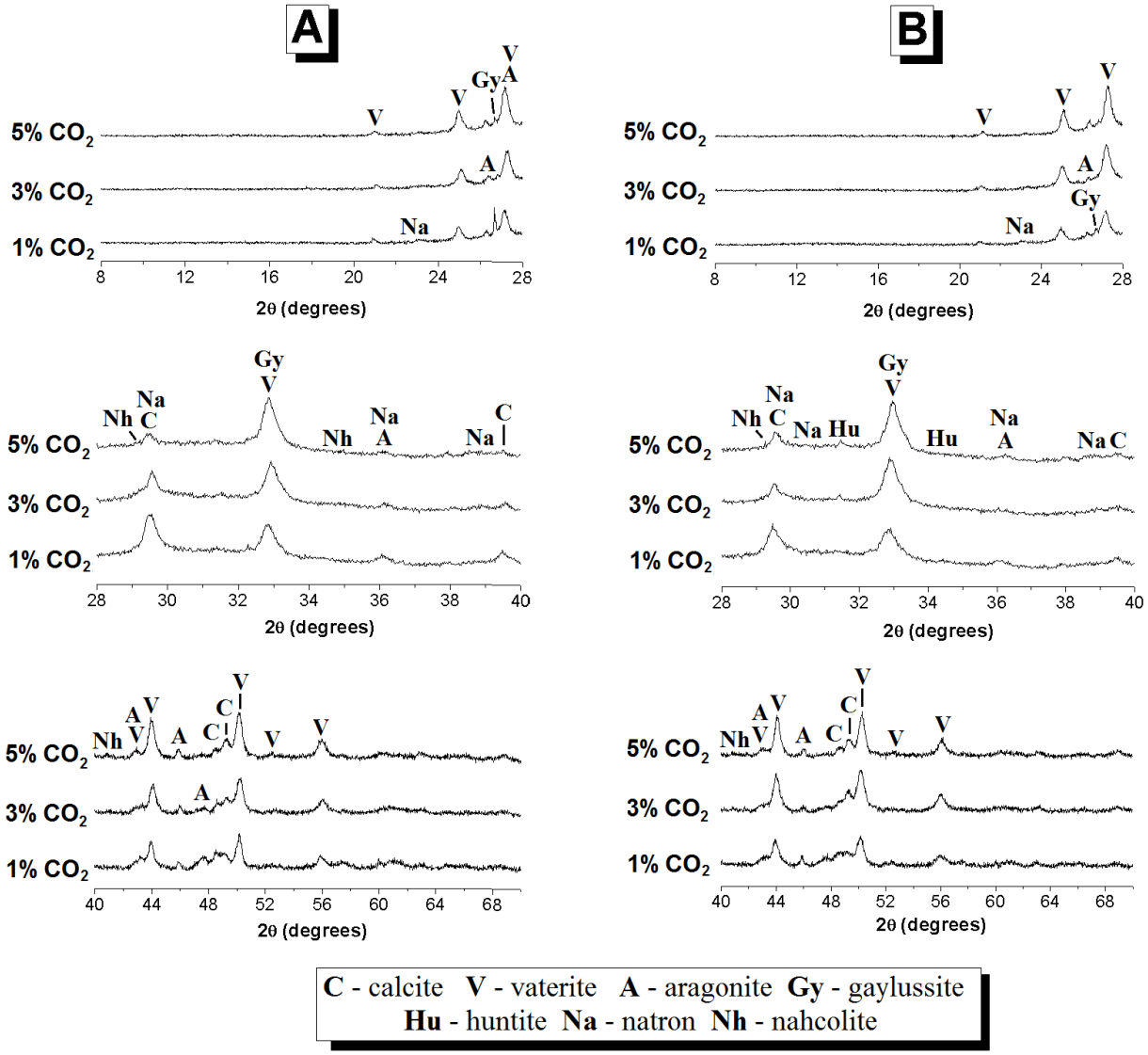

Figure 4. X-ray diffractograms of alkali-activated slag with (A) 1 day and (B) 7 days of curing, then exposed to elevated CO_2 concentrations as marked, for 7 days.

The presence of these three phases is in agreement with the discussion presented in [13], where it was identified that these systems seem to follow an Ostwald-type process whereby the least stable polymorph of $CaCO_3$ tends to crystallize first in these systems. This leads to the observation of the metastable $CaCO_3$ polymorphs vaterite and aragonite at higher CO_2 concentrations. The conversion to the more stable structure of calcite takes place more directly in those samples carbonated at the lower CO_2 concentrations, which is consistent with the formation of calcite as the main carbonation product in natural carbonated specimens [13]. In

7-day cured samples, huntite ($Mg_3Ca(CO_3)_4$, PDF# 00-014-0409) is also identified as a carbonation product, and its formation is likely to be associated with the carbonation of hydrotalcite.

The Na-rich carbonation products natron ($Na_2CO_3 \cdot 10H_2O$, PDF# 00-015-0800), nahcolite ($NaHCO_3$, PDF# 00-015-0700), and gaylussite ($Na_2Ca(CO_3)_2 \cdot 5H_2O$, PDF# 00-012-0255), are identified in carbonated samples. Detailed analysis of the formation of these phases is given elsewhere [13], where it is highlighted that the stability of the different Na-carbonate phases is strongly dependent on the accelerated carbonation conditions. At room temperature (23°C) and ambient CO_2 concentrations (~0.03-0.04%), natron is the most likely phase to form, while a CO_2 concentration exceeding 0.2% will promote the formation of nahcolite. Nahcolite has a much lower molar volume than natron [25], and will therefore provide a much lower degree of pore blockage to prevent the diffusion of CO_2 into the materials.

It was noted in [13] that this change in the solid phases also has a remarkable effect on the dissolved carbonate/bicarbonate equilibrium, which controls the pH of the carbonated pore solution, and consequently also the potential corrosion of steel reinforcement embedded in structural concretes. However, in the context of the current analysis, it is particularly important to note that the silicate gel structures which coexist in equilibrium with solutions of differing pH will also differ in chemistry and nanostructure, and this induces differences between natural and accelerated carbonation processes in alkali-activated binders. As the gels form and develop under high pH conditions during alkaline activation, they are more likely to remain thermodynamically stable under similar conditions, rather than when the pH is reduced by the acidification associated with high CO_2 partial pressures.

279 In the X-ray diffractograms of the alkali-activated fly ash samples after exposure to elevated
280 CO_2 concentrations (Figure 5) products of the carbonation of the pore solution are evident:
281 nahcolite in all samples, and sodium carbonate heptahydrate ($NaCO_3 \cdot 7H_2O$, PDF# 00-025-
282 0816) in the 1-day cured sample carbonated at 5% CO_2. The identification of nahcolite was
283 expected based on thermodynamic calculations of pore solution equilibria under elevated CO_2
284 conditions for sodium-rich pore solutions [13], and Figure 5 shows that it becomes more
285 prominent in the samples exposed at higher CO_2 partial pressures. However, the observation
286 of the heptahydrate phase, which is thermodynamically stable in a closed Na_2CO_3-$NaHCO_3$-
287 H_2O system only in a limited temperature range (32-35.4°C) [26] and at low pCO_2 [27] appears
288 to be unique in the literature for alkali-activated materials to date. The reasons and implications
289 of the formation of this phase will be explored in more detail in section 3.1.3.

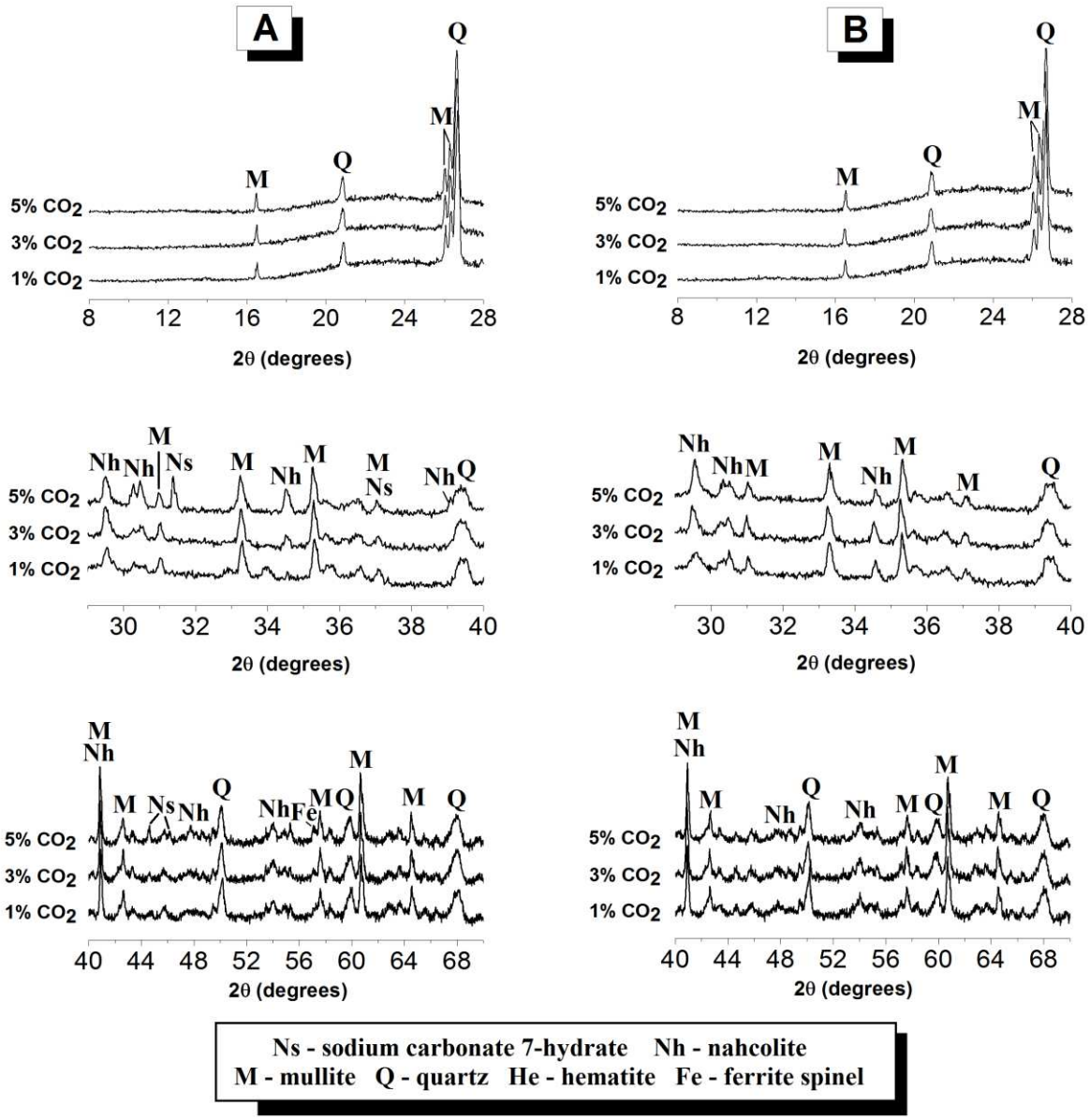

Figure 5. X-ray diffractograms of alkali-activated fly ash pastes cured for (A) 1 day or (B) 7 days, and exposed for 7 days to accelerated carbonation at different CO_2 concentrations as marked.

The carbonation of the blended fly ash-slag binders also leads to the formation of crystalline carbonate phases, as shown in Figure 6. It is particularly notable that no sodium-containing crystalline phases are formed in these systems; the carbonates observed are the three crystalline polymorphs of $CaCO_3$ (calcite, aragonite and vaterite), as well as the mixed Mg-Ca carbonate

phase huntite. These are the same phases that were identified in carbonated alkali-activated slag systems, but are observed in different proportions in the blended systems. In particular, huntite seems to be more prominent here than in the slag-only systems, particularly in the samples carbonated at 3% CO_2, and more so in the less-mature gels in Figure 6A than the more mature gels in Figure 6B. Huntite is less evident at 5% CO_2 at both ages, and it appears that the Mg has instead become incorporated into the calcite structure, seen via the shift to higher angle of the diffraction peaks assigned to this phase, as it is known that the inclusion of Mg in the calcite structure leads to a contraction of the unit cell [28].

Among the $CaCO_3$ phases observed here, and consistent with the results in the slag-only system, the content of vaterite increases with CO_2 concentration. According to the Ostwald step rule [29], vaterite would be expected to be the first crystalline polymorph of $CaCO_3$ to form during carbonation processes, as it is metastable with respect to calcite and aragonite [30]. The observation that it is most prominent at higher CO_2 concentration is therefore consistent with the details of the carbonation process here, as the duration of the CO_2 exposure was reasonably short. By comparison, calcite was the only $CaCO_3$ phase present after the carbonation of crushed alkali-activated slag pastes for 1000 h (approximately 6 weeks) at 3% CO_2 [9], as the metastable phases were fully converted to the most stable phase during this extended time. Aragonite is more prominent at 3% CO_2 than at 1% or 5% (as seen particularly by differences in the peak just below 46° 2θ); it was not observed at 5% CO_2 in the slag-only system, and only in a very small quantity here. The content of calcite is highest at 3% CO_2 here, whereas the content of this phase decreased with CO_2 concentration in slag-only binders carbonated under the same conditions.

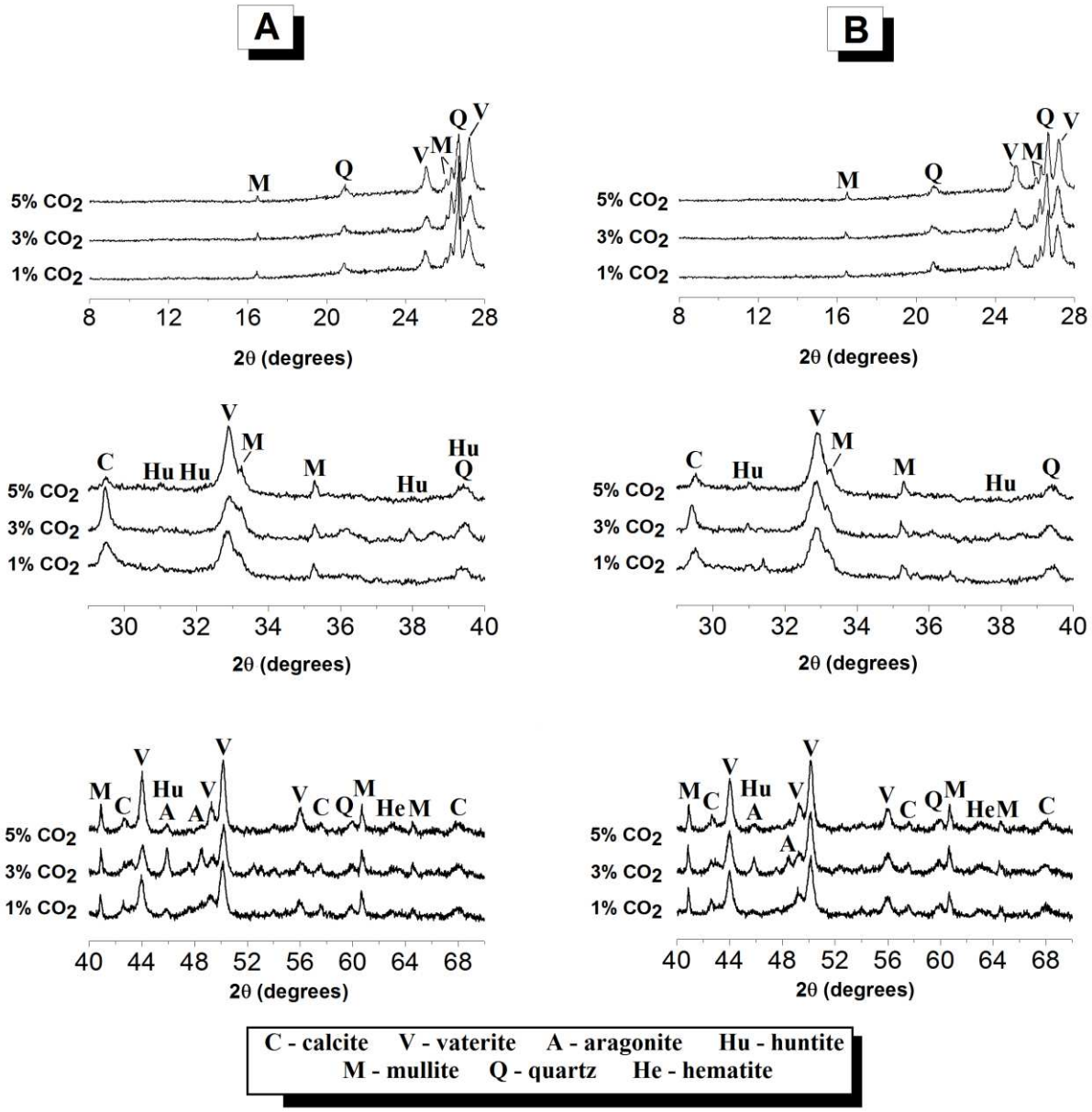

Figure 6. X-ray diffractograms of alkali-activated fly ash/slag blended pastes cured for (A) 1 day or (B) 7 days, and exposed for 7 days to accelerated carbonation at different CO_2 concentrations as marked.

3.1.3. Mechanism of CO_2 ingress and carbonate/bicarbonate precipitation

As was discussed in section 3.1.2, the phase $Na_2CO_3 \cdot 7H_2O$ was observed in only one sample: the alkali-activated fly ash sample with the lowest maturity, exposed at the highest CO_2

concentration, and this provides some important indications related to the mechanism of its formation. It is known that the phase equilibria in the Na_2CO_3-$NaHCO_3$-H_2O system are influenced by relative humidity [31], with intermediate hydration states of Na_2CO_3 (the monohydrate or heptahydrate) favoured over the decahydrate ($NaCO_3 \cdot 10H_2O$, natron) when the relative humidity is less than 100% and the temperature and CO_2 concentration are close to ambient. Combining this with the fact that elevated CO_2 concentrations lead to the formation of bicarbonates rather than carbonates, this behaviour suggests that the least-mature gel had a more rapid drop in internal relative humidity in the very early periods of CO_2 exposure, before a high concentration of CO_2 was able to diffuse into the internal parts of the pore network of the crushed particles. The 5% CO_2 environment was sufficient to induce an internal CO_2 concentration gradient within the crushed (-74 μm) particles, where the first carbonation of the interior of the sample takes place at a much lower CO_2 concentration than is present in the environmental chamber as a whole.

This is illustrated schematically in Figure 7, which shows an approximate relationship between CO_2 partial pressure in the gas contained within the pores and the depth from the surface of the particle. The CO_2 concentration in the outer, highly carbonated region is similar to the concentration in the environmental chamber, with a diffuse reaction zone then giving a gradual decrease in concentration. The kinetics of absorption of CO_2 into the alkaline pore solution determine the shape of the concentration profile within this region [32]. This profile is sharpened in the case of a more mature gel because the Thiele modulus (ratio of chemical reaction rate to diffusion rate [33]) must increase with gel maturity, as the diffusion becomes more hindered via the refinement of the pore network structure. The more mature gel has a much sharper interface, which corresponds more closely to the UR-CORE model proposed by

356 Castellote et al. [34] for Portland cement, which assumes a sharp interface (i.e. much more
357 rapid chemical reaction than diffusion, an infinite Thiele modulus). The shaded region in Figure
358 7 (corresponding to a CO_2 concentration low enough to give precipitation of carbonate rather
359 than bicarbonate salts) is much larger for the low-maturity gel at high CO_2 concentration than
360 in the other cases depicted. The alkali-rich pore solution may thus have carbonated directly to
361 form $Na_2CO_3 \cdot 7H_2O$, or alternatively initially to natron, converting to the heptahydrate when
362 the interior of the sample became dried under the controlled (65%) RH conditions of the
363 environmental chamber.

364

365

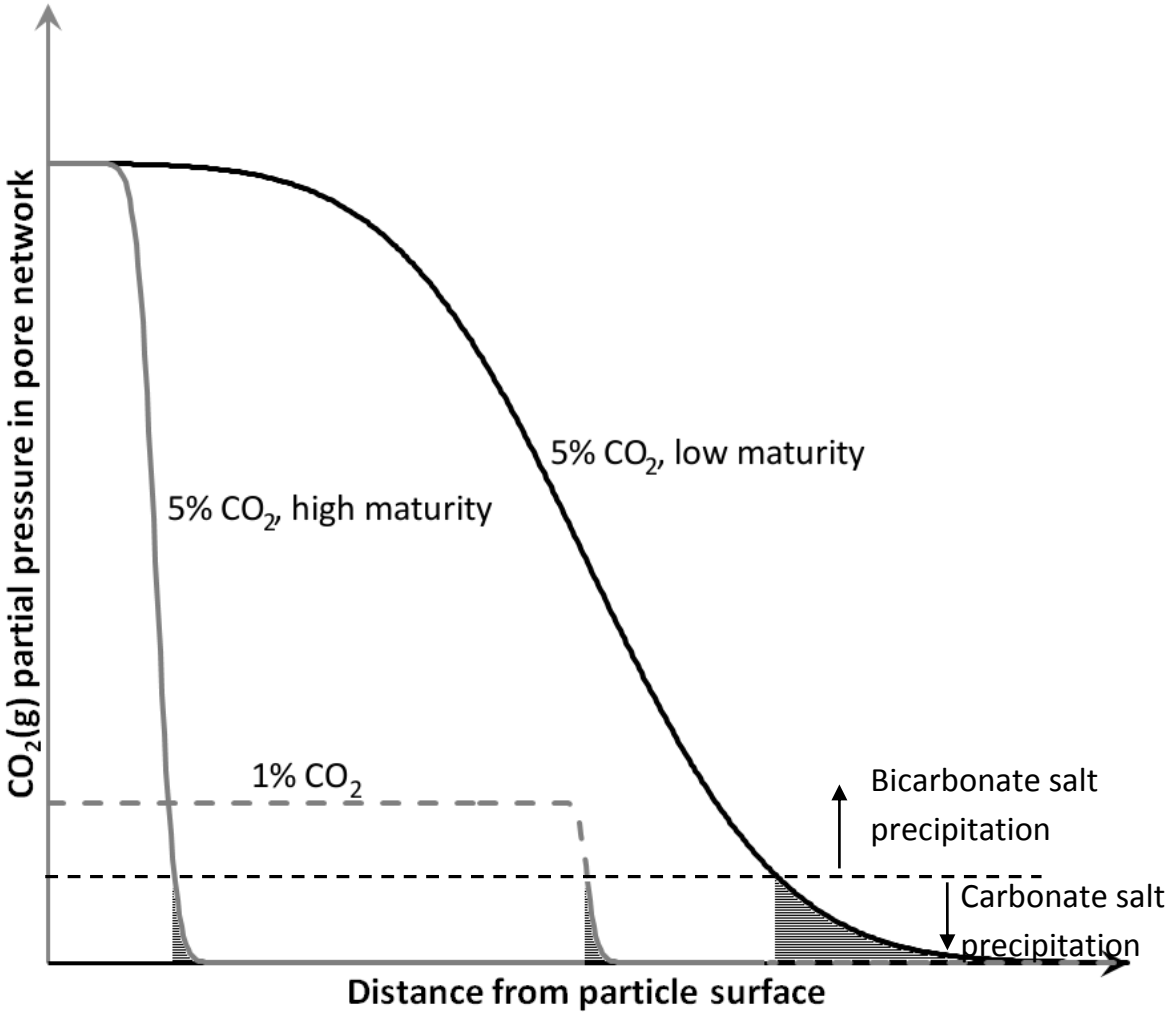

366

367 **Figure 7.** Schematic diagram showing the proposed mechanism of formation of sodium
368 carbonate heptahydrate (via natron) in the 5% CO_2, 1-day cured sample, but not in the other
369 samples tested. The curve for each sample indicates the shape of the CO_2 ingress front as it
370 enters the particles of each sample, and the shaded areas indicate the region in which
371 carbonate salts (natron and/or heptahydrate) will precipitate in each case.

372

373 The formation of sodium carbonate (rather than bicarbonate) salts must therefore occur in the
374 very early stages of the carbonation process, particularly in the crushed samples tested here
375 where the ingress of the carbonation front into the particles is rapid. However, the fact that the
376 relative humidity is sufficiently low to cause a drying front to enter the samples along with the
377 carbonation front [12] means that these precipitates are kinetically stabilised even after the CO_2

concentration in the particles equalises with the exterior environment, because the carbonate deposits are in contact with vapour rather than liquid, and thus their conversion to bicarbonates is slowed. In the longer-duration (1000 h) tests of Bernal et al. [9], the sodium carbonate product observed in alkali-activated slag systems was the mixed carbonate-bicarbonate salt trona, which is consistent with the mechanism proposed here, as this phase may be viewed as an intermediate in the conversion of carbonates to bicarbonates.

3.2. Thermogravimetry

Differential thermogravimetry data for carbonated and uncarbonated alkali-activated slag paste are shown in Figure 8. The mass loss from the uncarbonated binders (Figure 8A) takes place predominantly below 300°C, consistent with the release of the molecular water remaining in the pore structure of the material. The shoulder identified around 170°C is attributed to the first stage of the thermal dehydration of hydrotalcite [35], and this phase also contributes to the mass loss between 350-400°C. The progressive but notable mass loss in the region 250-350°C (where there is no sharp peak but the DTG trace deviates significantly from the baseline) is consistent with the presence of katoite and/or other hydrous calcium aluminate phases [36, 37]. The continuing dehydration of the C-S-H type gel is then observed via progressive mass loss above 380°C.

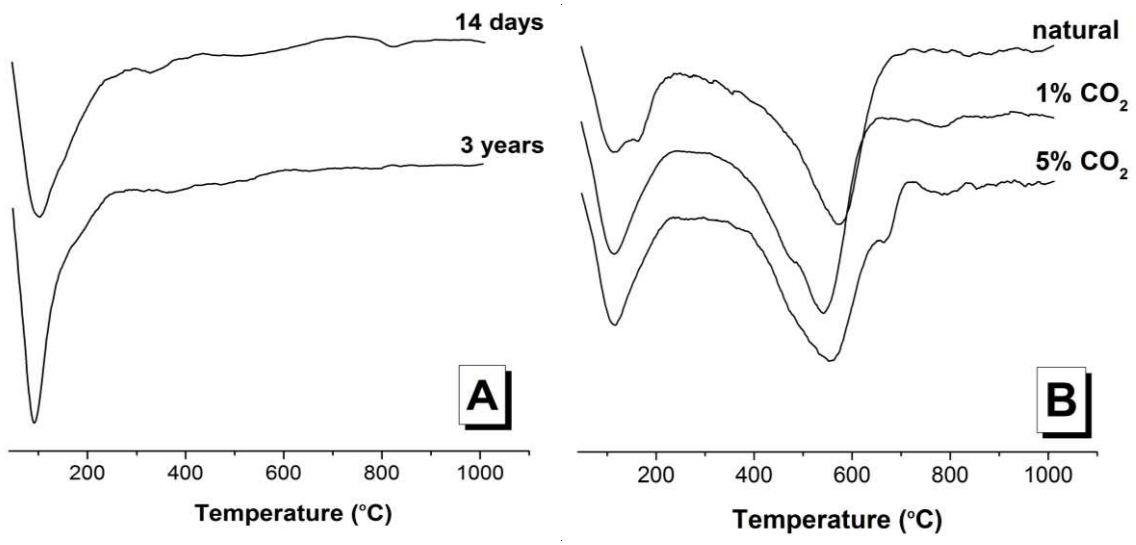

Figure 8. Differential thermograms (mass loss downwards) of (A) alkali-activated slag specimens, and (B) carbonated pastes (3 years natural carbonation, or 7 days of curing then 7 days of accelerated carbonation) as a function of the exposure conditions. The same vertical scale is used in (A) and (B).

In carbonated pastes (Figure 8B), a reduction in the intensity of the low temperature mass-loss peak assigned to the binder gel is identified. This effect seems to be more remarkable in naturally carbonated samples, where along with the reduction in mass loss intensity, the widening of this peak is observed, with the formation of a distinct secondary minimum at 162°C. This is related to the simultaneous dehydration of the binding gel and carbonation products. Considering that hydrotalcite (which also has a mass loss peak in this temperature range) is not observed in naturally carbonated pastes [13], it is likely that the second peak is associated with the dehydration of pirssonite ($Na_2Ca(CO_3)_2 \cdot 2H_2O$) and natron, which are only identified in the naturally carbonated paste [13]. The dehydration of double salts such as pirssonite and gaylussite takes place at temperatures below 250°C, with a maximum in the rate of mass loss in many such salts [38] taking place at a temperature consistent with the second peak identified in naturally carbonated alkali-activated slag paste in Figure 8. The dehydration of natron starts at temperatures below 60°C, but also shows a maximum in mass loss at ~160°C [39]. In the naturally carbonated paste, the mass loss peak observed in Figure 7B between

418 400°C and 700°C is mainly attributed to the thermal decomposition of calcite [9], which has
419 been identified as the main carbonation product in this sample [13], along with the minor
420 phases vaterite, aragonite, and huntite [40].
421
422 In alkali-activated slag pastes carbonated at 1% CO_2 and at 5% CO_2 (Figure 8B), a mass loss
423 peak at 117°C is identified, whose intensity is comparable for both of these accelerated
424 exposure conditions. Similar to the case in naturally carbonated specimens, this shows the
425 dehydration of the gel remaining after accelerated carbonation. The main differences induced
426 by the different CO_2 conditions are identified in the region corresponding to the decomposition
427 of the carbonate-rich phases (350 - 800ºC). In accelerated carbonated specimens, a shift in this
428 peak towards lower temperatures is observed. This is attributed to the formation of vaterite as
429 the main carbonation product in the accelerated carbonated sample, where the thermal
430 decomposition of this phase shows a peak centred at 560ºC [41]. The low intensity peak centred
431 at 657ºC observed in pastes carbonated at 5% CO_2 is likely to be associated with the thermal
432 decomposition of gaylussite, which has been identified predominantly in pastes carbonated at
433 higher CO_2 concentrations [13], and which decomposes at around 620ºC when heated in a CO_2-
434 free environment [38].
435
436 Figure 9 shows differential thermogravimetry data for selected carbonated and uncarbonated
437 alkali-activated fly ash and fly-ash/slag blended samples. The mass loss in the uncarbonated
438 binders takes place predominantly below 200°C, consistent with the presence of the water in
439 these samples mainly as molecular water within the binder pores. As was noted in section 2,
440 the samples were equilibrated under flowing N_2 for 60 minutes at 40°C prior to the start of
441 heating, meaning that free water in larger pores will have been lost during this period, and that
442 the water observed in the mass loss peak at ~150°C was either physisorbed or held in small

pores. Some water may also have been lost from hydrous carbonate phases in the carbonated samples during this equilibration time, as 40°C is above the transition temperature of natron or $Na_2CO_3 \cdot 7H_2O$ to thermonatrite ($Na_2CO_3 \cdot H_2O$).

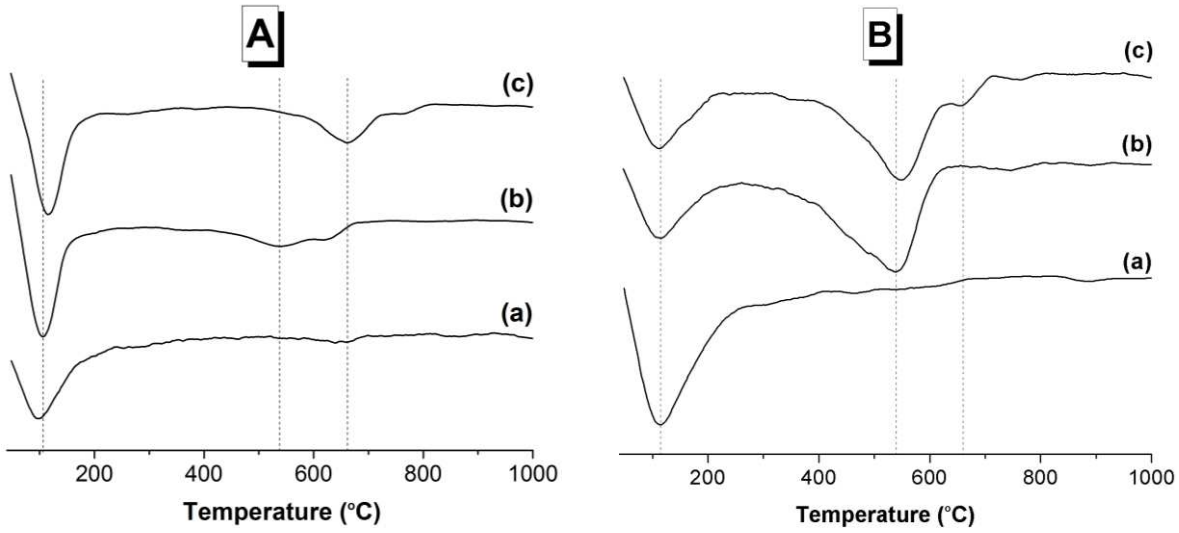

Figure 9. Differential thermograms (mass loss downwards) of alkali-activated (A) fly ash and (B) fly ash/slag binders with (a) 14 days of curing, and carbonated binders cured for 7 days then exposed to (b) 1% CO_2 and (c) 5% CO_2, for 7 days

In carbonated alkali-activated fly ash (Figure 9A**)**, there is an increase in the intensity of the mass loss peak around 150°C when compared with the uncarbonated binder. This overlaps with the loss of water from the binder, and the additional intensity is associated with the thermal conversion of nahcolite to Na_2CO_3 [42, 43]. The additional mass loss at higher temperature is attributed to decomposition of carbonates, by the release of CO_2. The Na_2CO_3 obtained through decomposition of $NaHCO_3$ is likely to be more reactive than that which is obtained through dehydration of sodium carbonates [44], which is consistent with the higher intensity of the highest-temperature mass loss peak (centred at 665ºC) in the sample exposed to 5% CO_2, which contains sodium carbonates as well as nahcolite.

In blended systems (Figure 9B**)**, carbonation leads to a reduction in the intensity of the low-temperature mass loss peak, indicating that there has been structural degradation of the gel during carbonation, with less scope to physically bind water in the degraded gel. A similar trend has been observed for slag-based binders exposed to accelerated carbonation (Figure 8). The fact that this was not observed in the fly ash-only binders in Figure 9A indicates that there was not a corresponding degree of gel degradation in the fly ash-based gel when exposed to carbonation, and this will be explored in more detail using NMR spectroscopy in section 3.3. It has previously been identified using X-ray microtomography that the gel in an alkali-activated 1:1 blend of fly ash and slag is more microstructurally similar to the slag-only system than the fly ash-only system [45], and it appears that this similarity also holds at the nanostructural (gel chemistry) level as probed by TGA.

In the blended binders, the intensity of the mass loss due to the remaining gel is comparable in pastes carbonated at 1% CO_2 and 5% CO_2, and the main differences induced by the different CO_2 conditions are identified in the region between 350ºC and 800ºC. The peak centred at 550ºC is consistent with the thermal decomposition of vaterite and huntite as identified by XRD in this sample, while the low intensity peak centred at 657ºC in pastes carbonated at 5% CO_2 is attributed to the thermal decomposition of calcite [9].

3.3. Nuclear magnetic resonance

3.3.1 Alkali-activated slag binders

Figure 10 shows ^{27}Al MAS NMR spectra of the alkali-activated slag binders, both with (Figure 10A) and without accelerated carbonation (Figure 10B). The spectrum of the unreacted slag

484 exhibits a broad resonance between 50 and 80 ppm and centred around 68 ppm, which is in the
485 region assigned to tetrahedral Al environments, but which cannot be assigned to a single well-
486 defined aluminium environment. This peak is attributed to the glassy phases composing the
487 majority of the slag, consistent with the amorphous hump and low crystalline phase content
488 identified in the slag by XRD (Figure 1). Upon activation, samples cured for 14 days show a
489 sharpening in this tetrahedral Al band when compared with the unreacted slag, along with the
490 formation of a somewhat narrower resonance centred at 74 ppm. The aluminium environments
491 resonating at ~68 ppm are associated with unreacted slag as discussed above, and also
492 potentially with the small number of Al atoms present in bridging tetrahedra within the C-S-H
493 gel which are bonded to the Q^3(1Al) silicate environments identified in Al-substituted
494 tobermorites [46], as discussed below. The narrow peak at 74 ppm is attributed to the
495 tetrahedrally coordinated Al incorporated in bridging tetrahedra bonded to Q^2(1Al) sites [46-
496 49]. Similar results are identified in the 3 year old paste in Figure 10A, consisting of a slight
497 increase in the intensity of the peak at 74 ppm and the asymmetrical broadening of the band
498 centred at 68 ppm, along with the formation of a low intensity band at ~58 ppm which appears
499 as a shoulder. The formation of a similar band has been observed in synthetic Al-substituted
500 tobermorites (C-A-S-H gels) with low Ca/(Si+Al) ratio, as a consequence of the increased
501 occupancy of Al(IV) in bridging tetrahedral sites [46].
502

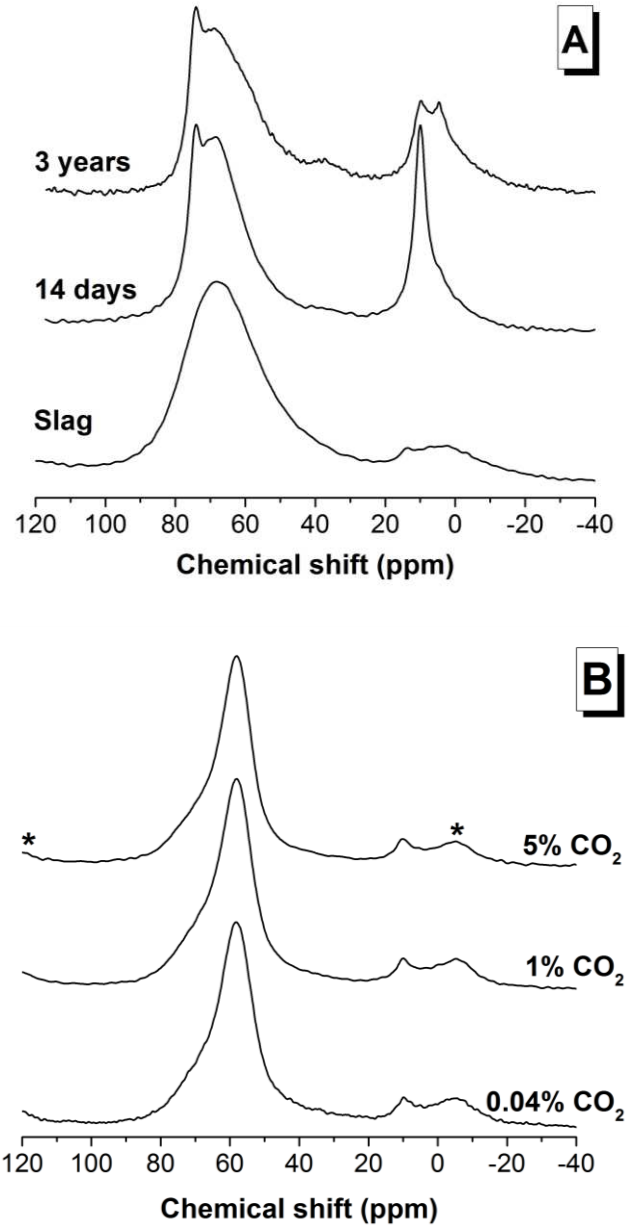

Figure 10. ^{27}Al MAS NMR spectra (14.1 T, ν_R=10 kHz) of (A) non-carbonated alkali-activated slags, and (B) carbonated specimens as a function of CO_2 exposure conditions (samples with 7 days of curing and 7 days of carbonation at 1% or 5% CO_2; the sample labelled as 0.04% CO_2 is the naturally carbonated sample exposed for three years). The asterisks (*) correspond to spinning side bands.

In the octahedral Al region (from -10 to 20 ppm), the alkali-activated slag sample cured for 14 days activated shows a high intensity narrow peak centred at 10 ppm, along with a small shoulder centred at 4.5 ppm. Peaks in these positions, and particularly around 10 ppm, have previously been assigned to both AFm and hydrotalcite-type phases [50, 51]. There is also a

minor contribution from Al(VI) in the unreacted slag, which is present in all spectra of uncarbonated and carbonated materials, but is not consistent with the structure or chemistry of either of the identifiable crystalline phases in the slag (gehlenite and åkermanite), and so must be assigned to an unreactive glassy component containing Al(VI).

The XRD data for these samples, as discussed in section 3.1, provide increased confidence in the assignment of these peaks. It has been suggested for alkali-activated binders [51] that the AFm type layers are formed in a partially-ordered manner in the interlayers of the tobermorite-like (C-A-S-H) structure, which means that it is difficult to identify this as a distinct structure. The peak associated with the Al(VI) sites in hydrotalcite-type compounds has been reported to occur at 2 ppm [52] or at 10 ppm [53], depending on the structure of the phase. Recent results reported by Sideris et al. [54] show that carbonate-containing hydrotalcite-like layered double hydroxides display resonances in both positions, with a high intensity peak at 11 ppm and a weaker shoulder at 3-4 ppm. Consequently, it is anticipated that this phase is contributing to the 10 ppm peak. Katoite also shows a resonance in this region, at around 12 ppm [55], while increasing substitution of silica into this structure leads to the appearance of a broad peak around 4 ppm [56], consistent with the shoulder observed here in a similar position.

In the 3 year old sample in Figure 10A, a remarkable reduction in the intensity of the 10 ppm peak is observed when compared with the 14 day sample, along with an increase in the intensity of the 3 ppm peak. The attribution of ^{27}Al NMR peaks at a chemical shift of approximately 3 ppm remains somewhat controversial in the cement chemistry literature [57], where such a resonance could be attributed either to the presence of one or more of the crystalline hydrate phases discussed above (but which are all more likely to show dominant resonances at around 10-12 ppm according to the literature), or to a disordered phase such as the ‘third aluminate

hydrate' of Andersen et al. [58, 59], which is a hydrous amorphous alumina structure. Here, because the contribution of the identifiable crystalline phases at 3 ppm is observed in each case to be less intense than their resonance at 10 ppm, the increase in the 3 ppm peak relative to the 10 ppm peak at later age is attributed to the formation of a disordered alumina-rich phase similar to the third aluminate hydrate at advanced age. The XRD data discussed in Section 3.1 indicate that the concentration of hydrotalcite appears to remain constant, and katoite becomes more prominent, at advanced age. Therefore, the reduction in the main octahedral Al peak is likely to be associated with the conversion of AFm-like structures to form this new hydrate product, with a corresponding reduction in the intensity of the 10 ppm peak.

The ^{27}Al MAS NMR spectra of carbonated samples (Figure 10B) show a similar lineshape independent of the concentration of CO_2 to which the samples were exposed. The disappearance of the peaks in the octahedrally coordinated Al region is particularly notable, although a small contribution from unreacted slag as noted above is still present. This indicates that these phases appear to be fully carbonated, which is consistent with the XRD results. The peak associated with Al(IV) in C-S-H is also diminished by carbonation; instead, a single band is identified in the Al(IV) region at ~58 ppm, indicating that the structure of the C-A-S-H type gel changes with carbonation towards a more crosslinked aluminosilicate structure. A small peak at 40 ppm in the uncarbonated specimens is assigned to Al(V) environments in the C-S-H type gel; this is greatly diminished by carbonation, consistent with the identified structural changes in this phase.

Figure 11 shows the ^{29}Si MAS NMR spectra of the unreacted slag, and alkali-activated slag after 14 days and 3 years of curing. The deconvolution of the overlapped peaks was carried out using Gaussian line shapes for quantification, and the component peaks and simulated spectra

565 are shown along with the experimental data in Figure 11. The deconvolutions were performed
566 in Microsoft Excel by including the minimum possible number of component peaks to describe
567 the spectrum accurately (no more than 7 for reaction products), and constraining peak widths
568 to be <10 ppm full width at half height (FWHH). Peaks are assigned to connectivity states
569 based on information available in the literature for cements [48, 60] and for aluminosilicate
570 zeolite systems [61], and peak positions and widths are held constant throughout the
571 deconvolutions of all systems. In conducting the deconvolution of the spectra, it was assumed
572 that the lineshape of the remnant anhydrous slag does not change during the time of reaction,
573 and so the spectrum of the unreacted slag was rescaled by a single factor in each spectrum, to
574 provide the appropriate contribution in this region. The spectrum of the unreacted slag (Figure
575 11A), with an overall maximum at -76 ppm, is consistent with results for åkermanite glass [62],
576 in good agreement with the identification of this compound by XRD in the slag used in this
577 study. A recent study [63] has shown that this method is the most suitable for quantification of
578 ^{29}Si MAS NMR spectra of alkali-activated slags and blended cements containing slag, enabling
579 direct calculation of the extent of reaction.
580

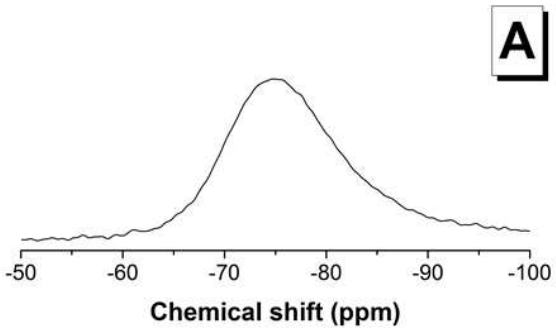

581

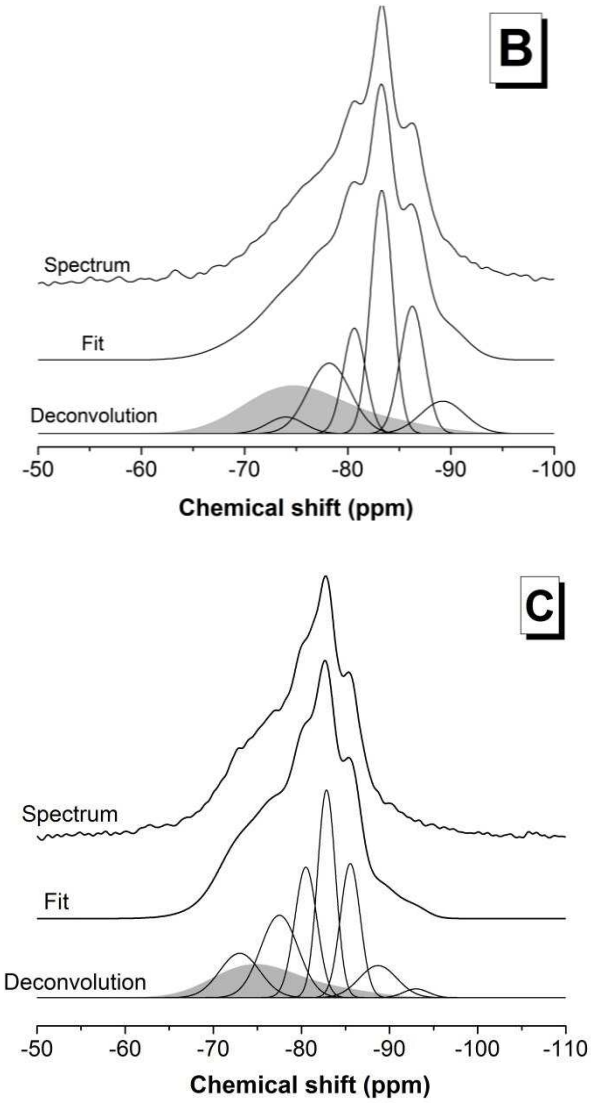

582

583

584 **Figure 11.** ^{29}Si MAS NMR spectra (14.1 T, ν_R=10 kHz) of (A) anhydrous slag, (B) alkali-
585 activated slag cured for 14 days, and (C) alkali-activated slag cured for 3 years. In spectra B
586 and C, the fit is the sum of the deconvoluted peaks, and the dark grey band represents the
587 contribution of the remnant anhydrous slag.

588

589 The resonances at –77 ppm and –80 ppm in 14 day cured alkali-activated slag pastes (Figure
590 11B) are attributed to the presence of two different types of Q^1 sites in the C-S-H type gel
591 formed as the main reaction product in these systems. Le Saoût et al. [63] assign a peak at -
592 75.8 ppm in alkali-silicate activated slags to either Q^0 or Q^1(1Al) sites; however, the Q^1 sites
593 in C-S-H gels can either be bonded to Si or Al, and can also have different ratios of Ca^{2+}, Na^+
594 and H^+ in charge-balancing sites. Thus, there are multiple distinct possibilities in terms of

595 bonding environments of non-bridging oxygens which may influence the ^{29}Si chemical shift of
596 a Q^1 site, rather than this simply being determined by whether the single bridging oxygen atom
597 is linked to Si or Al. This possibility was considered in a model for synthetic tobermorite-like
598 C-S-H gels proposed by Rejmak et al. [64], where some of the $SiO(OH)^+$ units were removed
599 and the excess negative charge neutralised with protons or Ca^{2+} ions. The variation in charge-
600 balancing species can influence the ^{29}Si MAS NMR chemical shift, and suggests that the
601 assignment of the Q^1 peak region in alkali-activated slag binders is not straightforward. As a
602 simplification in this study, the Q^1 region of each spectrum, between -70 and -80 ppm, has been
603 deconvoluted into two peaks, which are denoted as Q^1(a) and Q^1(b) respectively, without
604 specifically assigning each to a particular chemical environment.
605
606 Resonances at –82 ppm and -84 ppm are also observed in activated slag pastes, corresponding
607 to Q^2(1Al) and Q^2 sites, consistent with the formation of an Al-substituted C-S-H type (C-A-
608 S-H) gel with a tobermorite type structure. However, it is important to note that the C-A-S-H
609 gel formed by alkali-activation of this slag also shows peaks at –89 ppm and -93 ppm assigned
610 to Al-substituted Q^3 and Q^4 species, which will overlap in the spectra. This is consistent with
611 the structural model and interpretation of ^{29}Si MAS NMR results recently proposed by the
612 authors [65] where a highly crosslinked C-N-A-S-H type gel has been identified in these
613 systems after extended curing. The appearance of this band is consistent with previous studies
614 of sodium silicate-activated and sodium carbonate-activated slag binders [6, 20, 46, 66], which
615 have solely attributed it to a Q^3(1Al) component.
616
617 This is consistent with the presence of the 58 ppm peak in the ^{27}Al MAS NMR spectra of these
618 specimens (Figure 4), and the observations presented by other authors [20, 67] in analysis of
619 silicate-activated slags, showing the formation of crosslinked tobermorites with Al(IV)-O-Si

linkages. The C-A-S-H gels formed in sodium silicate-activated slag are thus more polymerised than conventional Portland cement binders, where Q^3 sites are not generally identified [68]. The quantification of the different Q^n sites for the noncarbonated pastes is presented in Table 2.

Table 2. Summary and quantification of Q^n environments identified in ^{29}Si MAS NMR spectra of uncarbonated alkali-activated slag (AAS) pastes. Estimated uncertainty in site percentages is ± 1%.

Sample ID	Site type and chemical shift (ppm)							
		Activated slag reaction products						
	Unreacted slag	Q^0	Q^1(a)	Q^1(b)	Q^2(1Al)	Q^2	Q^3(1Al); Q^4(nAl)	
		-74	-78	-80	-83	-86	-89	-93
Unreacted slag	100%							
AAS – 14 days	25%	3%	14%	11%	25%	15%	7%	
AAS – 3 years	17%	9%	17%	15%	20%	14%	6%	1%

It can be observed from Table 2 that there is a reduction in the fraction of sites assigned to unreacted slag over the time of curing (from 25% at 14 days to 17% at 3 years). In 3 year old activated slag paste, there is a significant increase in the intensity of the Q^0 and Q^1 sites, along with a reduction in the intensity of the Q^2(1Al) band and an increase in the Q^2 sites, when compared with the 14 day samples. The increase in the prevalence of Q^0 and Q^1 sites is consistent with the formation of katoite type phases, as previously identified by XRD. The structure of katoite is based on Si sites which share oxygen atoms with four octahedrally coordinated Al sites, and so registers in the region of the NMR spectrum consistent with Q^0 or

Q^1 Si environments [55]. The reduction in the intensity of Q^2(1Al) may also be a consequence of these structural changes, as Al is increasingly incorporated into phases other than C-A-S-H as the reaction progresses.

The ^{29}Si MAS NMR spectra of carbonated alkali-activated slag pastes, along with deconvolutions and fits, are shown in Figure 12, with quantification presented in Table 3. Remarkable differences between natural and accelerated carbonated pastes are identified, when comparing Figures 11 and 12, or Tables 2 and 3. However, there is not a significant difference between the ^{29}Si MAS NMR spectra of the accelerated carbonated specimens exposed to 1% CO_2 or 5% CO_2. The extent of structural changes in the accelerated carbonated pastes is notably more severe than in the naturally carbonated pastes. This is most evident when examining the degradation of the chain (Q^1 and Q^2) structure of the gel and formation of a more cross-linked (and probably decalcified) gel, as shown in Figure 11. In all carbonated samples, the peak associated with Q^2(1Al) sites is no longer identifiable, and the formation of a highly crosslinked aluminosilicate type gel is evident, consistent with the ^{27}Al MAS NMR results.

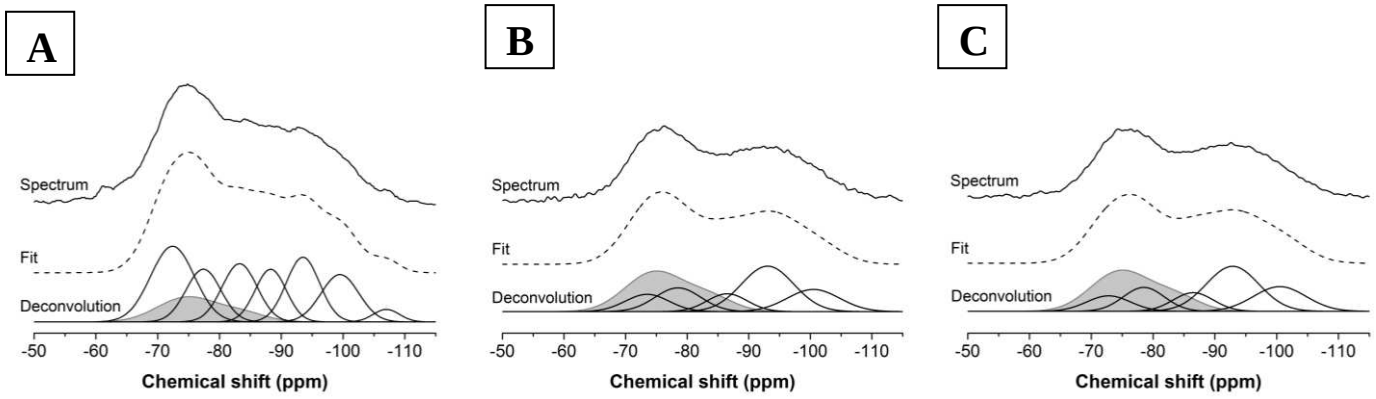

Figure 12. Deconvoluted ^{29}Si MAS NMR spectra (14.1 T, ν_R=10 kHz) of (A) naturally carbonated alkali-activated slag after 3 years of exposure, and accelerated carbonated pastes cured for 7 days then exposed to (B) 1% CO_2, or (C) 5% CO_2, for 7 days.

658

659 **Table 3.** Summary of Q^n environments identified in ^{29}Si MAS NMR spectra of carbonated
660 alkali-activated slag (AAS) pastes. Estimated uncertainty in site percentages is ± 1%.

Sample ID	Site type							
		Activated slag reaction products and carbonation products						
	Unreacted slag	Q^0	Q^1	Q^2	Q^4(4Al)	Q^4(3Al)	Q^4(2Al)	Q^4
		-72	-77	-83	-88	-93	-100	-107
AAS – Naturally carbonated	12%	22%	12%	14%	11%	14%	12%	2%
AAS – 1% CO_2	33%	8%	12%	-	8%	26%	13%	-
AAS - 5% CO_2	33%	8%	11%		8%	26%	14%	-

661

662

663 3.4.2 Alkali-activated fly ash and blended binders

664 Figure 13 shows ^{29}Si MAS NMR spectra of the fly ash and the binders derived from its alkali
665 activation, before and after carbonation. The spectrum of the reacted binder is very similar to
666 that of the fly ash, as both the unreacted glassy phases in the ash and the binder gel contain a
667 distribution of Q^4(nAl) sites, with n between 0 and 4, as identified and quantified in Table 4.
668 Each spectrum is deconvoluted into component Gaussian peaks for quantification as described
669 in section 3.4.1, and the component peaks and the simulated spectra are shown along with the
670 experimental data in Figure 13. A further guideline applied in the deconvolution procedure of
671 the fly ash-derived systems was that the intensities of adjacent peaks should vary smoothly,
672 rather than having a particular Q^4(nAl) site with an intensity which is either much higher or
673 much lower than that of the neighbouring (n+1 or n-1) sites. This principle was introduced on
674 the basis of the thermodynamics of a statistical distribution of Si and Al sites within a Q^4 (glass

675 or gel) network [69]; although the site populations were not calculated directly from such a
676 distribution, this principle was used to ensure that the site populations were meaningful.

677

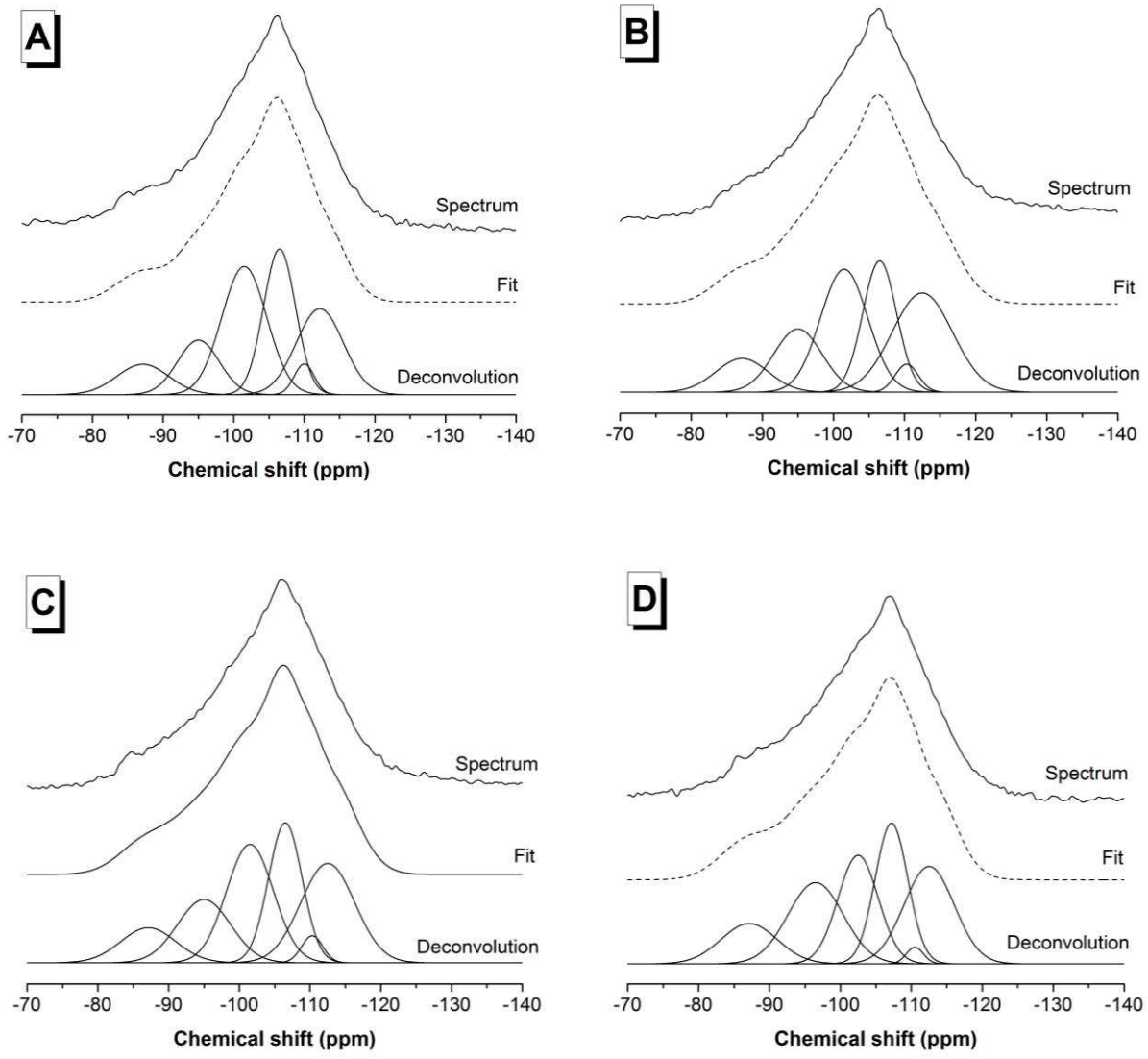

678 **Figure 13.** ^{29}Si MAS NMR spectra of (A) unreacted fly ash, (B) alkali-activated fly ash cured
679 for 14 days, and 7-day cured alkali-activated fly ash exposed at (C) 1% CO_2 and (D) 5% CO_2
680 for 7 days.

681

682 **Table 4.** Deconvolution results of ^{29}Si MAS NMR spectra of alkali-activated fly ash pastes
683 before and after carbonation. Estimated uncertainty in site percentages is ± 1%.

Sample ID	Site type				
	Q^4(4Al)	**Q^4(3Al)**	**Q^4(2Al)**	**Q^4(1Al)**	**Q^4(0Al)**
Chemical shift (ppm)	-87	-97	-102	-107	-113
Unreacted FA	9%	12%	32%	25%	22%
Activated FA	8%	15%	28%	21%	28%
Carbonated 1% CO_2	9%	16%	27%	22%	26%
Carbonated 5% CO_2	11%	21%	22%	22%	24%

The deconvolutions also show a small, sharp peak at -112 ppm, which remains unchanged between all samples studied and is not listed in Table 4. This is attributed to the unreactive mullite and quartz present in the fly ash. Based on this identification, the intensity of this peak is excluded from the quantification of the different Si species identified in the material – partly because the material is unreactive and therefore not part of the binder, and partly because the very long relaxation delays associated with the Q^4 sites in quartz (exceeding 1 hour [70, 71]) means that they will not be captured quantitatively in the spectra here, where a 20 s relaxation delay was used. Although mullite is also expected to give some contribution to the intensity around -87 ppm and -106 ppm [72], this has not been considered separately in the quantification.

Figure 13 and Table 4 show that there is only a very slight change in the silicon environments in the alkali-activated fly ash system as a result of carbonation. The deconvolution results show a slight increment in the intensities of the Q^4(4Al) and Q^4(3Al) sites with carbonation of the paste, which is more significant with exposure to higher CO_2 concentrations. The intensities of the Q^4(2Al) and Q^4(0Al) peaks are reduced with carbonation, and this is more significant with the exposure to higher CO_2 concentrations. No significant variations are identified in the

intensities of the Q^4(1Al) sites, which may be related to the contribution of the remnant mullite in the system at this chemical shift. The stability of the chemistry of the alkali-activated fly ash gel under these conditions is quite remarkable, particularly considering that the chemistry and pH of the pore solution present within the gel have been altered so strongly by the high CO_2 concentrations, as shown in the XRD data in section 3.1 of this paper, as well as through the thermodynamic modelling presented in [13].

It is noted that although the gel structure of alkali-activated fly ash does not seem to be changed very much upon carbonation, these pastes were easily destroyed by hand after accelerated carbonation exposure. This change in structural performance, which is likely to be related to extensive cracking due to the aggressive exposure conditions, indicates that the changes taking place in this gel cannot fully be detected in the nanostructural characterisation. Further characterisation work in this area is undoubtedly necessary.

The situation for the blended fly ash-slag binders, as shown in Figure 14, is somewhat different. The deconvolution and quantification of the spectra of the blend of raw materials, the reacted materials and the carbonated binders are given in Table 5. The reaction products of the slag are much more readily distinguishable from the unreacted raw material than is the case for the fly ash, and so Table 5 shows the unreacted slag and slag reaction products separate from each other, but the fly ash and its reaction products are not able to be separated in this way.

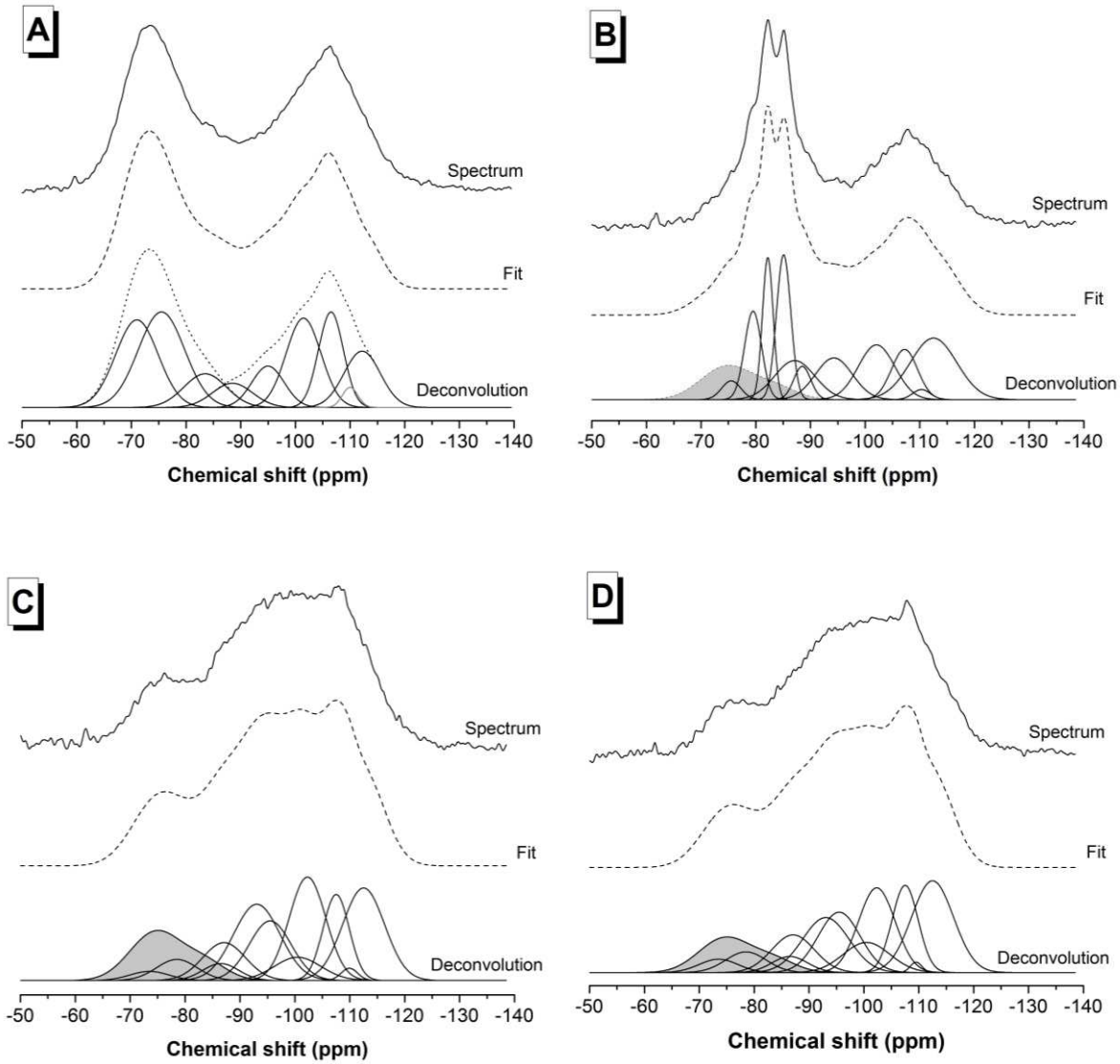

723 **Figure 14.** ^{29}Si MAS NMR spectra of (A) unreacted fly ash/slag blend, (B) alkali-activated
724 fly ash/slag blend cured for 14 days, and the 7-day cured alkali-activated fly ash/slag blend
725 exposed at (C) 1% CO_2 and (D) 5% CO_2 for 7 days. In the deconvolutions of the reacted
726 materials, the contribution of the unreacted slag is shaded in grey.

727

Table 5. Deconvolution of results of ^{29}Si MAS NMR spectra of alkali-activated fly ash/slag blended pastes before and after carbonation. Relative intensities are reported in brackets. The peak at -112 ppm, assigned to mullite and quartz in the unreacted fly ash, is excluded from the quantification. Estimated uncertainty in site percentages is ± 1%.

Sample ID	Site type												
	Unreacted slag	Activated slag reaction products								Fly ash and reaction products				
		Q^1(a)	Q^1(b)	Q^2(1Al)	Q^2	Q^3(1Al)	Q^4(4Al)	Q^4(3Al)	Q^4(2Al)	Q^4(4Al)	Q^4(3Al)	Q^4(2Al)	Q^4(1Al)	Q^4(0Al)
Unreacted FA/GBFS blend	49%									-87 (5%)	-97 (7%)	-102 (16%)	-107 (12%)	-113 (11%)
Activated FA/GBFS blend	13%	-76 (2%)	-80 (9%)	-82 (9%)	-85 (12%)	-89 (3%)	-	-	-	-87 (9%)	-96 (9%)	-102 (11%)	-107 (7%)	-113 (16%)
Carbonated 1% CO_2	13%	-74 (1%)	-79 (4%)	-	-	-	-87 (3%)	-93 (15%)	-101 (5%)	-87 (7%)	-96 (11%)	-102 (16%)	-108 (9%)	-113 (16%)
Carbonated 5% CO_2	11%	-74 (2%)	-79 (4%)	-	-	-	-87 (3%)	-93 (12%)	-101 (6%)	-87 (7%)	-96 (12%)	-102 (14%)	-108 (11%)	-113 (18%)

870 The blended binders (Figure 14) show distinct differences in binder structure compared to pure
871 alkali-activated slag binders (Figure 11) formulated and cured under the same conditions. The
872 prevalence of Q^2 sites (Table 5) in the blended binders is notably higher than would be expected
873 if the presence of fly ash did not have any influence on the reaction of the slag, and the Q^1 and
874 Q^2(1Al) sites are much less prominent. This is attributed in part to a dilution effect, where the
875 less-reactive fly ash does not consume as much of the silicate activator, leading to an effectively
876 higher availability of the activator for reaction with the slag. As the activator supplies Si, but
877 not Al, the higher activator availability will reduce the Si/Al ratio compared to the slag-only
878 binder. However, because this C-A-S-H type gel does not bind the alkalis as strongly as the N-
879 A-S-H ('geopolymer') type gel which forms from the fly ash, the ongoing interaction of the fly
880 ash with the Na supplied by the activator can lead to the formation of N-A-S-H gel. By
881 comparing the deconvolution results for the fly ash-derived sites in the blended binder in Table
882 5 with the equivalent sites in the fly ash-only binder in Table 4, it is apparent that the reaction
883 of fly ash in the blended binder leads to a higher proportion of Q^4(4Al) and Q^4(3Al) sites than
884 in the fly ash-only binder. This is consistent with the consumption of silica from the activator
885 by more rapid reaction with the slag, leaving an alkali-rich but silica-poor activating solution
886 available to react with the fly ash, thus giving a more Al-rich gel reaction product.

887

888 The spectra (Figure 14) and deconvolutions (Table 5) show that carbonation in blended systems
889 induces decalcification of the C-S-H type reaction products, which result from the interaction
890 of the slag with the activator. This leads to the precipitation of calcium carbonates, as identified
891 by XRD in Figure 6, and the formation of a residual aluminosilicate type gel mainly comprised
892 of Al-substituted Q^4 sites (Table 5). In calculating the deconvolutions presented in Table 5, the
893 peak positions assigned to the fly ash reaction products were held as close to constant as

possible, because these peaks were changed only slightly by carbonation, and the new intensity in the Q^4(nAl) region is thus assigned to the products of carbonation of the slag-derived gel.

Carbonation also influences the reaction products derived from the activation of the fly ash, but to a much lower extent than in the reaction products derived from the activation of the slag, consistent with the results for the fly ash-only binders shown in Table 4. It is difficult to identify a clear trend in the effect of the CO_2 concentration on the fly ash reaction products. A slight reduction in the contribution of Q^4(4Al) is identified, along with an increased contribution of the Q^4(3Al), Q^4(2Al) and Q^4(1Al) sites. It is also noted that the Q^4(nAl) sites identified as being formed through carbonation of the slag-derived gel have chemical shifts which differ slightly from those of the corresponding fly ash-derived peaks. The chemical shift values for the carbonated slag-gel peaks are thus identified here by matching as closely as possible the peak positions and widths obtained through deconvolution of the spectra of carbonated alkali-activated slags, and then fitting the intensities to match the experimental spectrum of the blended binder.

Figure 15 shows ^{27}Al MAS NMR spectra of the alkali-activated fly ash materials, with and without accelerated carbonation exposure (Figure 15A), and the corresponding data for the fly ash/slag blended binders (Figure 15B). The fly ash contains broad peaks due to octahedral (-20 to 30 ppm) and tetrahedral (30 to 75 ppm) Al sites, where the octahedral sites correspond to Al in mullite and in mullite-like glassy phases [73], and the tetrahedral sites are Al substituted in silicate glasses [74]. Upon alkaline activation, the shape of the octahedral peak is altered, with the loss of intensity at around 0 ppm leaving a residual peak which appears to have shifted to a more negative chemical shift. This apparent shift reflects the selective reaction of the sites

with chemical shift close to 0 ppm rather than the more shielded (-10 to -20 ppm) sites, and the conversion of these relatively reactive sites to tetrahedral coordination, as seen by the increased intensity of the Al(IV) peak. This peak also shows an increased contribution from a relatively narrow resonance at 50 ppm, due to the Al(IV) sites in the highly crosslinked alkali aluminosilicate gel [74]. At the relatively high field (14.1 T) and fast spinning rate (10 kHz) used here, this peak is well-resolved and distinct from the underlying broad signal due to the fly ash. The carbonation of the alkali-activated fly ash binder leads to almost no change in the ^{27}Al MAS NMR spectra as shown in Figure 15A; this is consistent with the observations for these samples from ^{29}Si MAS NMR.

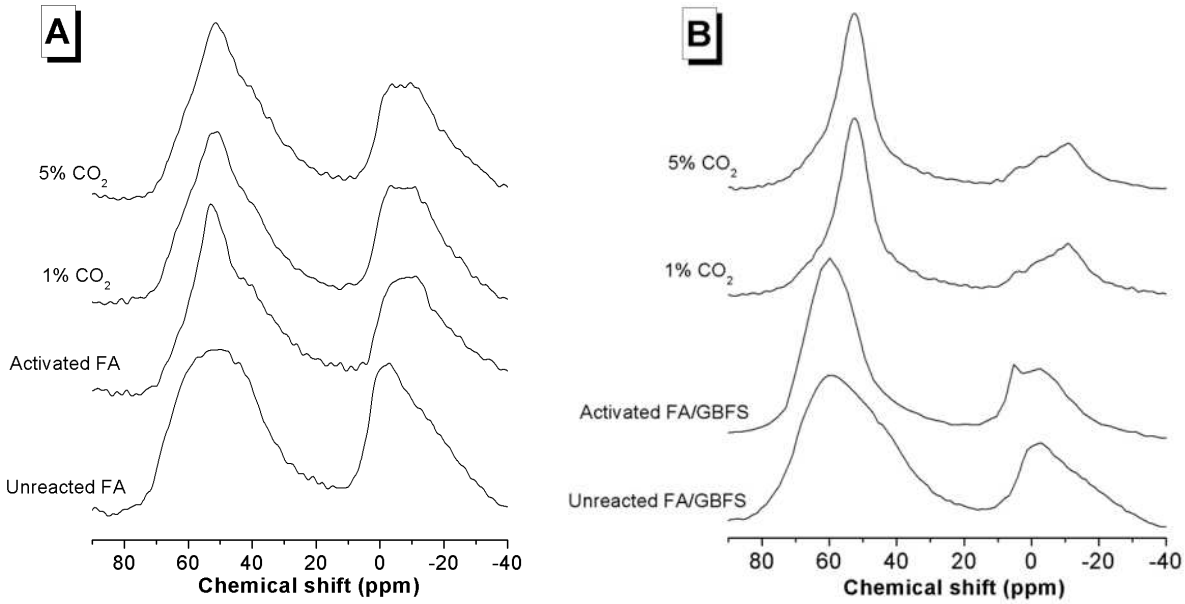

Figure 15. ^{27}Al MAS NMR spectra of (A) alkali-activated fly ash and (B) alkali-activated fly ash/slag blends.

Figure 15B shows that the alkali-activated fly ash-slag binder also contains both Al(IV) and Al(VI) sites. The Al(IV) region shows a peak which is somewhat broader than the distinct feature in the spectra in Figure 15A, and its position and breadth are consistent with the

presence of Al(IV) sites in both N-A-S-H type and C-A-S-H type gels, superimposed on an underlying feature due to unreacted raw materials. The Al(VI) region also shows the presence of partially reacted precursor materials, along with a sharp feature at 5 ppm which is attributed to the presence of Al(VI) in nanostructured octahedral environments resembling the third aluminate hydrate phase, hydrotalcite and/or katoite, as in the alkali-activated slag binders discussed above. Such phases were not identifiable by XRD in these samples (Figure 3), indicating that they are either disordered, or intimately intermixed with the C-A-S-H gel, or both. These Al(VI) environments are influenced by carbonation of the binder, as the intensity in this region of the spectra is reduced with exposure to elevated CO_2 concentrations, consistent with the data for the slag-only binder systems. The peak at -10 ppm in these spectra is a spinning sideband associated with the Al(IV) peak.

The most notable change in the spectra of the blended binders with carbonation is in the Al(IV) region. It was observed from the ^{29}Si MAS NMR spectra that the blended binder contains Si environments which are able to be assigned to both C-A-S-H and N-A-S-H type gels, and that the C-A-S-H environments are more prone to changes under exposure to elevated CO_2 conditions. The ^{27}Al spectra in Figure 15B are consistent with this observation, as there is an effective movement of the intensity in this region to lower chemical shift. The Al(IV) sites in C-A-S-H type gels display a resonance at higher chemical shift than the Al(IV) sites in N-A-S-H gels [46, 75]. This indicates that the broad peak observed in the uncarbonated binder is comprised of a contribution at high chemical shift (~ 65 ppm) from the C-A-S-H gel and another at lower chemical shift (~55 ppm) from the N-A-S-H gel, overlaid on the contribution of the unreacted precursors. With carbonation, the high chemical shift (C-A-S-H) peak is essentially removed, similar to the observations for this gel in ^{29}Si MAS NMR, leaving the

contribution of the N-A-S-H gel essentially unchanged, as in the fly ash-only samples in Figure 15A.

3.4. Scanning electron microscopy

A backscattered electron micrograph of an accelerated carbonated alkali-activated slag sample, cured for 7 days and then exposed to 5% CO_2 for 7 days, is shown in Figure 16. Here the unreacted slag (light grey), residual binder (medium grey) and carbonated regions (dark grey) are all clearly visible. The carbonation and decalcification of the C-A-S-H gel causes an increase in the concentration of C and O atoms, which have a lower elemental number than the other elements prevalent in C-A-S-H, resulting in a darkening of the greyscale image in the carbonated regions. Distinct carbonated regions are distributed throughout the binding gel and close to the unreacted slag grains, promoting the formation of microcracks in the carbonated regions. The shrinkage caused by decalcification is known to cause cracking as a consequence of the induced mechanical stress [76], sometimes referred to as carbonation shrinkage. It is notable that the carbonated regions tend to be close to the slag grains, and the 'inner product' regions (immediately surrounding slag particles) in alkali-activated slag binders show a denser gel structure than the 'outer product' (further from the remnant precursor grains) regions [77]. As such, further insight into the spatially heterogeneous nature of the binder gel is necessary to provide a suitable explanation for these observations.

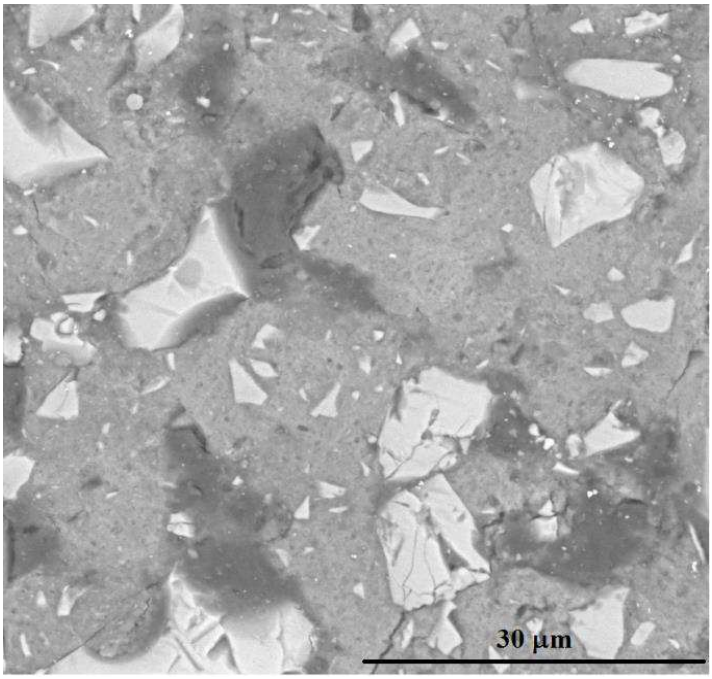

Figure 16. Backscattered electron image of alkali-activated slag cured for 7 days then exposed for 7 days at 5% CO_2.

A summary of the results of EDX analysis of the designated carbonated and uncarbonated regions is reported in Figure 17, showing that the carbonation of the gel leads to a reduction in the Ca/Si ratio, consistent with the decalcification of the gels through the formation of carbonates. This is accompanied by a reduction in the Mg/Si and Al/Si ratios in the carbonated regions. Wang and Scrivener [50] noted that the overall Al/Si ratio as measured by EDX considers a significant amount of Al present in reaction products other than C-A-S-H gel, such as hydrotalcite, katoite and AFm phases, as discussed above. After carbonation, according to the XRD and NMR data, hydrotalcite and AFm type phases seem to be completely consumed, consistent with the reduction in the Mg/Si and Al/Si ratios of the reaction products in Figure 17.

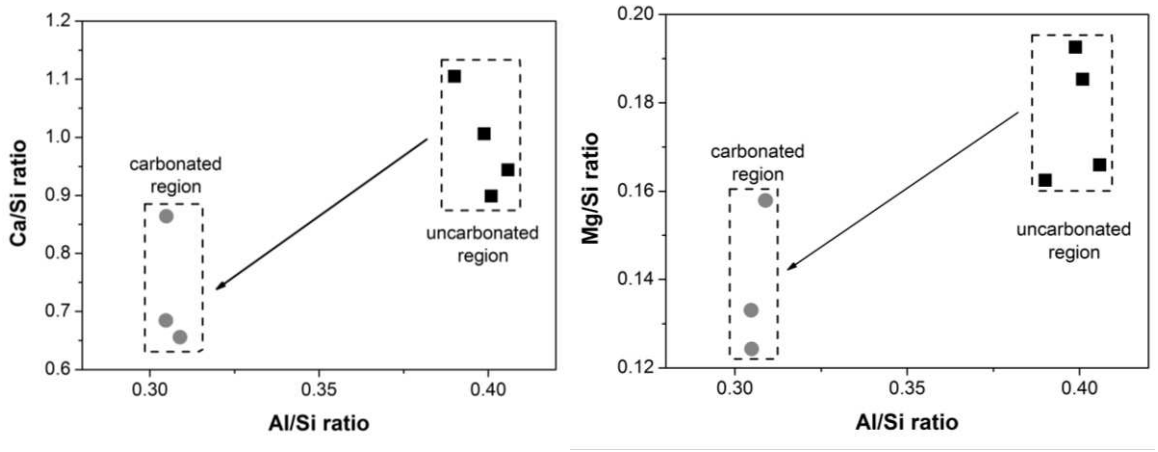

Figure 17. Atomic ratios Ca/Si vs Al/Si and Mg/Si vs Al/Si, for uncarbonated and carbonated regions identified in Figure 16 and other images of the same sample.

A scanning electron micrograph, and elemental maps obtained using EDX, of an alkali-activated fly ash binder are shown in Figure 18. The carbon elemental map shows that this element is distributed throughout the binder regions, presumably through carbonate precipitation from the pore solution. The unreacted fly ash particles are rich in aluminium and silicon, and are distinct from the binder (which has broadly similar chemical composition) because the unreacted particles are dense while the binder is porous. The sodium is distributed throughout the binder, as well as being concentrated in some of the remnant fly ash particles, most likely in partially-reacted glassy phases. There does not seem to be a strong correlation between the location of the carbon and any of the other elements when considering only the binder regions; it appears that the binder is sufficiently porous that the carbonated pore solution is distributed throughout the material.

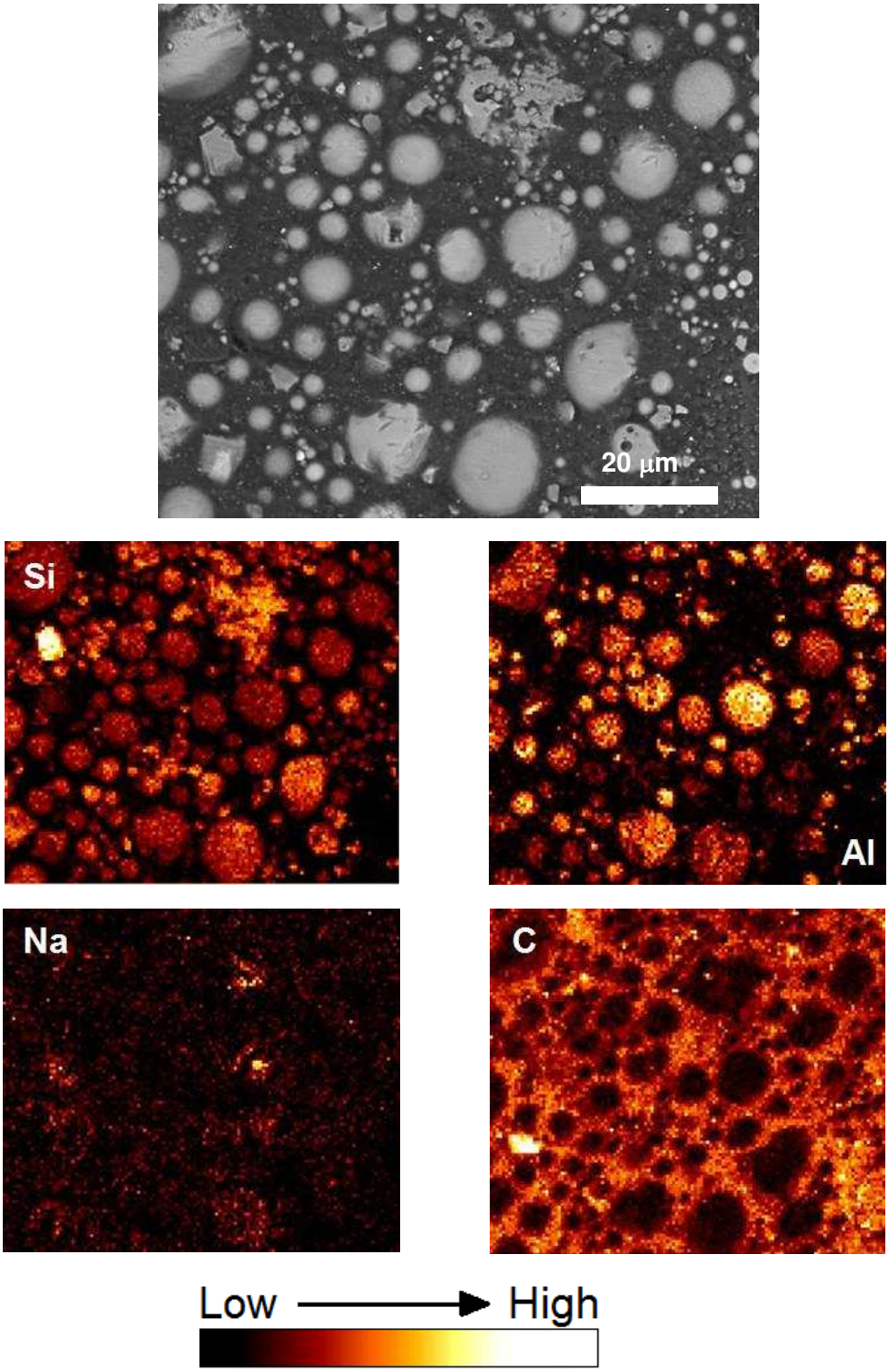

Figure 18. Backscattered electron image and elemental maps of alkali-activated fly ash carbonated at 5% CO_2. The elemental maps show the same region as the backscattered electron image.

1015 Figure 19 shows corresponding BSE and elemental maps for the blended binder. In these
1016 images, there appears to be a relatively strong correlation between the binder regions with high
1017 Ca content and those with low C content, indicating that the higher-Ca binder regions (mainly
1018 surrounding the residual slag particle in the centre of the region shown here) contain a lower
1019 concentration of carbonate reaction products.

1020

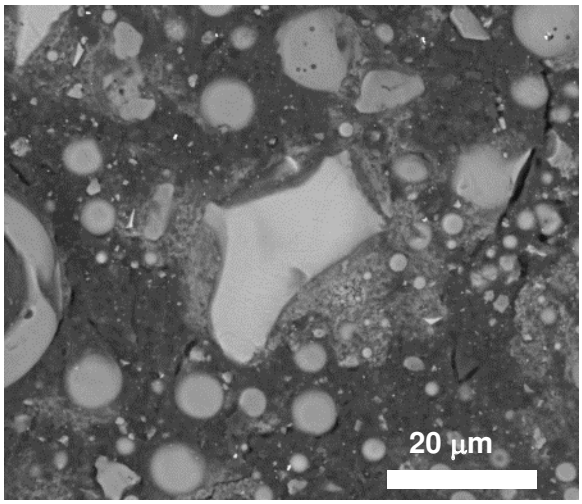

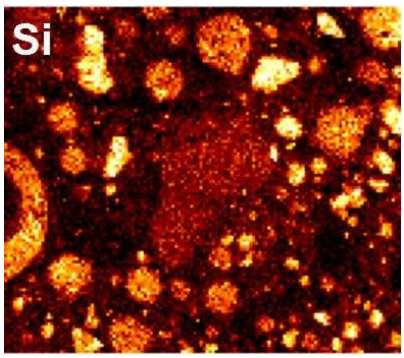

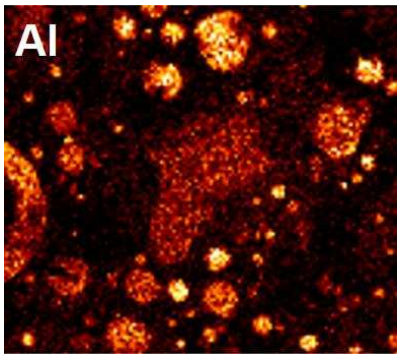

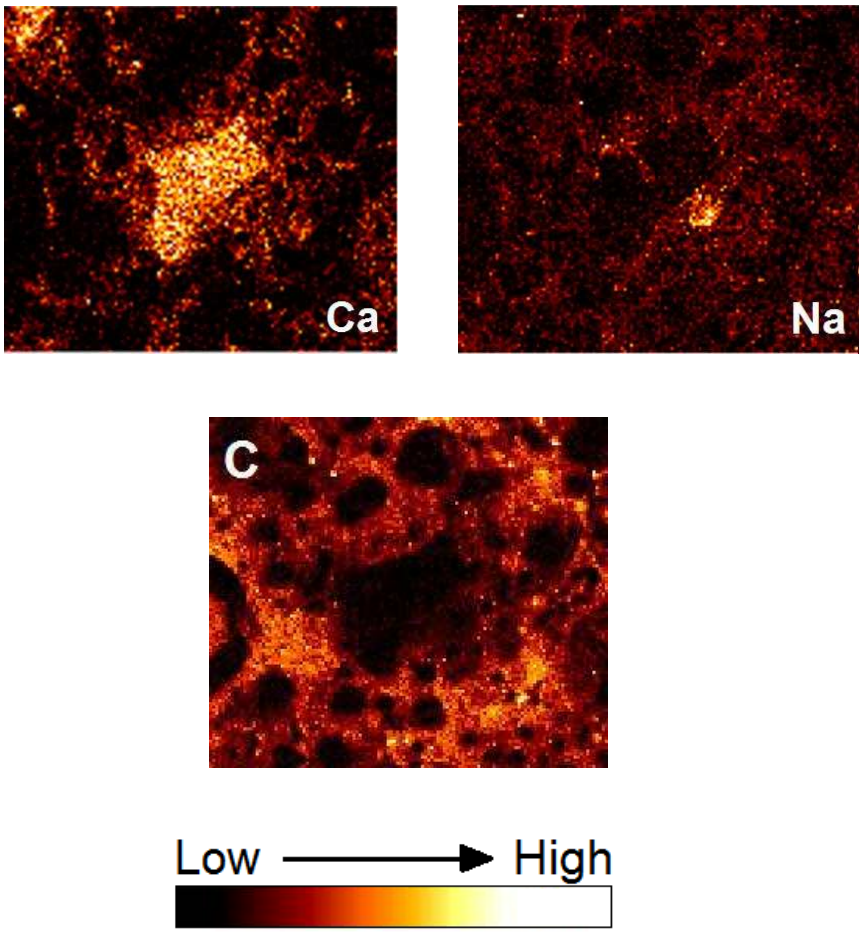

Figure 19. Backscattered electron image and elemental maps of alkali activated fly ash/slag blends carbonated at 5% CO_2. The elemental maps show the same region as the backscattered electron image.

This is consistent with the higher space-filling character of the products of alkaline activation of slag than of fly ash [45], and shows that the relationship between the extent of nanostructural change in the gel induced by exposure to elevated CO_2 concentrations and the extent of 'carbonation' (as described by the quantity of carbonate reaction products formed), is different between the two types of gel present. The N-A-S-H gel is more porous, contains highly alkaline pore solution which is relatively readily carbonated, but is almost unaltered on a nanostructural level by this process. The C-A-S-H type gel is less porous, and less readily carbonated as

measured by the deposition of carbonates from its pore solution, but shows a much greater degree of structural alteration due to the decalcification associated with carbonation.

This information, combined with the spectroscopic information presented throughout this paper, gives a detailed overview of the process of accelerated carbonation of alkali-activated binders on a nanostructural level, and importantly, the differences between natural and accelerated carbonation processes. In addition to the severity of the microstructural changes induced by carbonation at higher CO_2 concentrations (>1%), an unrepresentative disruption of the pore network, along with the changes in pore solution pH induced at elevated CO_2 concentrations [13], will also cause more extensive chemical damage to the silicate gel structure. Both natural and accelerated carbonation lead to degradation of secondary phases containing Al(VI) environments, which are mainly hydrous alkali earth aluminates in the slag-containing systems studied, while N-A-S-H gel structures are not strongly altered. However, accelerated carbonation is far more damaging than natural service conditions to the aluminosilicate chain structure of the C-S-H type binder gel, and so it is essential to interpret the results of accelerated carbonation tests with caution. Accelerated carbonation tests of alkali-activated materials should be understood as indicators enabling comparison of binder quality among a set of materials of comparable chemistry, but with care and considering the limited accuracy achievable in estimating 'real life' performance of the material from the results obtained.

4. Conclusions

Characterisation of the nanostructural effects of exposure of alkali-activated slag to elevated CO_2 concentrations has shown important differences between the progress, and reaction products, when compared with natural (ambient) CO_2 exposure. The hydrous alkali earth

aluminate phases present in alkali-activated slag binders (hydrotalcite, katoite, AFm type phases and amorphous hydrous aluminates) are carbonated under all exposure conditions. Conversely, the carbonation-induced reactions of the tobermorite-like layered silicate gel, which is the predominant phase in these materials, differ notably as a function of CO_2 concentration. This is due to a number of mechanisms, including differences in the pH of the pore solution which is held in the gel structure, and changes in the alkali carbonate/bicarbonate phase equilibria as a function of exposure conditions. Nuclear magnetic resonance spectroscopy is sensitive to changes in gel structure, where the decalcification of the carbonated gel leads to a higher degree of cross-linking and the loss of its chain-like character, particularly at high CO_2 concentrations. Conducting accelerated carbonation testing using CO_2 concentrations beyond ~1% CO_2 will not accurately replicate the mechanisms observed in service.

Alkali-activated fly ash-based binders carbonate mainly through precipitation of alkali bicarbonate salts from the pore solution, with almost no change to the binder gel as measured by thermogravimetry and NMR analysis of coordination states of the Si and Al in the network. Some fly ash-based binders also show indications of a diffuse carbonation reaction zone, particularly in samples with an immature gel when exposed to a high CO_2 concentration. Sodium metasilicate-activated fly ash/slag blends contain two distinct types of binder gel, one of which resembles the C-A-S-H gel formed through alkali silicate activation of slag, and the other of which is an N-A-S-H gel. Under accelerated carbonation exposure, these gels each respond according to a similar mechanism as observed in the sole-precursor binder systems, leaving a crosslinked, remnant silicate phase derived from decalcification of the C-A-S-H gel, coexisting with the largely unaltered N-A-S-H gel resulting from activation of fly ash, as well as various alkali and alkali-earth carbonate precipitates.

These results are essential in the understanding of carbonation of alkali-activated binders in service, particularly in the context of the laboratory analysis of carbonation. Such analysis is generally conducted at high CO_2 concentrations, and so is likely to provide unrepresentative or misleading results if the exposure conditions are not carefully controlled to provide the closest possible correlation to natural exposure conditions.

5. Acknowledgements

This work has been funded by the Australian Research Council, through a Linkage Project co-sponsored by Zeobond Pty Ltd, and also including partial funding through the Particulate Fluids Processing Centre. We also wish to acknowledge the Advanced Microscopy Facility at The University of Melbourne for assistance with the electron microscopy experiments conducted in this study, particularly Mr Roger Curtain in the use of the Micro-Analysis facilities.

6. References

[1] C. Shi, P.V. Krivenko, D.M. Roy, Alkali-Activated Cements and Concretes, Taylor & Francis, Abingdon, UK, 2006.

[2] J.S.J. van Deventer, J.L. Provis, P. Duxson, Technical and commercial progress in the adoption of geopolymer cement, Miner Eng, 29 (2012) 89-104.

[3] J.S.J. van Deventer, J.L. Provis, P. Duxson, D.G. Brice, Chemical research and climate change as drivers in the commercial adoption of alkali activated materials, Waste Biomass Valoriz, 1 (2010) 145-155.

[4] EN 13295:2004: Products and systems for the protection and repair of concrete structures – test methods – Determination of resistance to carbonation.

[5] M.A. Sanjuán, C. Andrade, M. Cheyrezy, Concrete carbonation test in natural and accelerated conditions, Adv Cem Res, 15 (2003) 171 - 180.

[6] M. Palacios, F. Puertas, Effect of carbonation on alkali-activated slag paste, J Am Ceram Soc, 89 (2006) 3211-3221.

[7] J. Deja, Carbonation aspects of alkali activated slag mortars and concretes, Silic Industr, 67 (2002) 37-42.

[8] K. Byfors, V. Klingstedt, P.Y.Y. Lehtonen, L. Rombern, Durability of concrete made with alkali activated slag, in: 3rd International Conference on Fly Ash, Silica Fume, Slag and Natural Pozzolans in Concrete, American Concrete Institute, Trondheim, Norway, 1989, 1429-1444.

[9] S.A. Bernal, R. Mejía de Gutierrez, V. Rose, J.L. Provis, Effect of silicate modulus and metakaolin incorporation on the carbonation of alkali silicate-activated slags, Cem Concr Res, 40 (2010) 898-907.

[10] E. Rodríguez, S. Bernal, R. Mejía de Gutierrez, F. Puertas, Alternative concrete based on alkali-activated slag, Mater Constr, 58 (2008) 53-67.

[11] D.W.S. Ho, R.K. Lewis, Carbonation of concrete and its prediction, Cem Concr Res, 17 (1987) 489-504.

[12] S.A. Bernal, J.L. Provis, R. Mejia de Gutierrez, J.S.J. van Deventer, Accelerated carbonation testing of alkali-activated slag/metakaolin blended concretes: effect of exposure conditions, Cem Concr Res, (2012) Submitted.

[13] S.A. Bernal, J.L. Provis, D.G. Brice, A. Kilcullen, P. Duxson, J.S.J. van Deventer, Accelerated carbonation testing of alkali-activated binders significantly underestimate the real service life: The role of the pore solution, Cem Concr Res, 42 (2012) 1317-1326.

[14] I. Lecomte, M. Liégeois, A. Rulmont, R. Cloots, F. Maseri, Synthesis and characterization of new inorganic polymeric composites based on kaolin or white clay and on ground-granulated blast furnace slag, J Mater Res, 18 (2003) 2571-2579.

[15] C. Li, H. Sun, L. Li, A review: The comparison between alkali-activated slag (Si+Ca) and metakaolin (Si+Al) cements, Cem Concr Res, 40 (2010) 1341-1349.

[16] M. Criado, A. Palomo, A. Fernández-Jiménez, Alkali activation of fly ashes. Part 1: Effect of curing conditions on the carbonation of the reaction products, Fuel, 84 (2005) 2048-2054.

[17] J. Bijen, H. Waltje, Alkali activated slag-fly ash cements, in: 3rd International Conference on Fly Ash, Silica Fume, Slag and Natural Pozzolans in Concrete, ACI SP114, Trondheim, Norway, 1989, 1565-1578.

[18] R.P. Williams, A. van Riessen, Determination of the reactive component of fly ashes for geopolymer production using XRF and XRD, Fuel, 89 (2010) 3683-3692.

[19] M. Ben Haha, B. Lothenbach, G. Le Saout, F. Winnefeld, Influence of slag chemistry on the hydration of alkali-activated blast-furnace slag -- Part I: Effect of MgO, Cem Concr Res, 41 (2011) 955-963.

[20] A. Fernández-Jiménez, F. Puertas, I. Sobrados, J. Sanz, Structure of calcium silicate hydrates formed in alkaline-activated slag: Influence of the type of alkaline activator, J Am Ceram Soc, 86 (2003) 1389-1394.

[21] S.D. Wang, K.L. Scrivener, Hydration products of alkali-activated slag cement, Cem Concr Res, 25 (1995) 561-571.

[22] I.G. Richardson, A.R. Brough, G.W. Groves, C.M. Dobson, The characterization of hardened alkali-activated blast-furnace slag pastes and the nature of the calcium silicate hydrate (C-S-H) paste, Cem Concr Res, 24 (1994) 813-829.

[23] F. Bonk, J. Schneider, M.A. Cincotto, H. Panepucci, Characterization by multinuclear high-resolution NMR of hydration products in activated blast-furnace slag pastes, J Am Ceram Soc, 86 (2003) 1712-1719.

[24] J.L. Provis, G.C. Lukey, J.S.J. van Deventer, Do geopolymers actually contain nanocrystalline zeolites? - A reexamination of existing results, Chem Mater, 17 (2005) 3075-3085.

[25] Institute of Experimental Mineralogy of the Russian Academy of Sciences, WWW-MINCRYST: Crystallographic and Crystallochemical Database for Minerals and their Structural Analogues, 2011, http://database.iem.ac.ru/mincryst/index.phppp.

[26] R.C. Wells, D.J. McAdam, Phase relations of the system: sodium carbonate and water, J Am Chem Soc, 29 (1907) 721-727.

[27] C. Monnin, J. Schott, Determination of the solubility products of sodium carbonate minerals and an application to trona deposition in Lake Magadi (Kenya), Geochim Cosmochim Acta, 48 (1984) 571-581.

[28] J.R. Goldsmith, D.L. Graf, Relation between lattice constants and composition of the Ca-Mg carbonates, Am Miner, 43 (1958) 84-101.

[29] A. Navrotsky, Energetic clues to pathways to biomineralization: Precursors, clusters, and nanoparticles, Prod Nat Acad Sci USA, 101 (2004) 12096-12101.

[30] A. Sarkar, S. Mahapatra, Synthesis of all crystalline phases of anhydrous calcium carbonate, Cryst Growth Des, 10 (2010) 2129-2135.

[31] H. Haynes, R. O'Neill, M. Neff, P.K. Mehta, Salt weathering of concrete by sodium carbonate and sodium chloride, ACI Mater J, 107 (2010) 258-266.

[32] C.Y. Wen, Noncatalytic heterogeneous solid-fluid reaction models, Ind Eng Chem, 60 (1968) 34-54.

[33] O. Levenspiel, Chemical Reaction Engineering, 3rd Ed., Wiley, New York, 1999.

[34] M. Castellote, C. Andrade, Modelling the carbonation of cementitious matrixes by means of the unreacted-core model, UR-CORE, Cem Concr Res, 38 (2008) 1374-1384.

[35] F. Rey, V. Fornes, J.M. Rojo, Thermal decomposition of hydrotalcites. An infrared and nuclear magnetic resonance spectroscopic study, J Chem Soc Faraday Trans, 88 (1992) 2233-2238.

[36] J.M. Rivas-Mercury, P. Pena, A.H. de Aza, X. Turrillas, Dehydration of $Ca_3Al_2(SiO_4)_y(OH)_{4(3-y)}$ ($0<y<0.176$) studied by neutron thermodiffractometry, J Eur Ceram Soc, 28 (2008) 1737-1748.

[37] V.S. Ramachandran, C.-M. Zhang, Thermal analysis of the $3CaO\cdot Al_2O_3$-$CaSO_4\cdot 2H_2O$-$CaCO_3$-H_2O system, Thermochim Acta, 106 (1986) 273-282.

[38] D.R. Johnson, W.A. Robb, Gaylussite: Thermal properties by simultaneous thermal analysis, Am Mineral 58 (1973) 778-784.

[39] S.K. Sharma, C.K. Jotshi, S. Kumar, Thermal stability of sodium salt hydrates for solar energy storage applications, Sol Energy, 45 (1990) 177-181.

[40] L.A. Hollingbery, T.R. Hull, The thermal decomposition of huntite and hydromagnesite - A review, Thermochim Acta, 509 (2010) 1-11.

[41] M. Maciejewski, H.-R. Oswald, A. Reller, Thermal transformations of vaterite and calcite, Thermochim Acta, 234 (1994) 315-328.

[42] E.M. Barall, L.B. Rogers, Differential thermal analysis of the decomposition of sodium bicarbonate and its simple double salts, J Inorg Nucl Chem, 28 (1966) 41-51.

[43] P.K. Heda, D. Dollimore, K.S. Alexander, D. Chen, E. Law, P. Bicknell, A method of assessing solid state reactivity illustrated by thermal decomposition experiments on sodium bicarbonate, Thermochim Acta, 255 (1995) 255-272.

[44] K. Mocek, D. Beruto, On the morphological nature of Na_2CO_3 produced by thermal decomposition from $NaHCO_3$ and from $Na_2CO_3\cdot 10H_2O$, Mater Chem Phys, 14 (1986) 219-227.

[45] J.L. Provis, R.J. Myers, C.E. White, V. Rose, J.S.J. van Deventer, X-ray microtomography shows pore structure and tortuosity in alkali-activated binders, Cem Concr Res, 42 (2012) 855-864.

[46] G.K. Sun, J.F. Young, R.J. Kirkpatrick, The role of Al in C-S-H: NMR, XRD, and compositional results for precipitated samples, Cem Concr Res 36 (2006) 18-29.

[47] M.D. Andersen, H.J. Jakobsen, J. Skibsted, Incorporation of aluminum in the calcium silicate hydrate (C−S−H) of hydrated Portland cements: A high-field ^{27}Al and ^{29}Si MAS NMR investigation, Inorg Chem, 42 (2003) 2280-2287.

[48] I.G. Richardson, A.R. Brough, R. Brydson, G.W. Groves, C.M. Dobson, Location of aluminum in substituted calcium silicate hydrate (C-S-H) gels as determined by ^{29}Si and ^{27}Al NMR and EELS, J Am Ceram Soc, 76 (1993) 2285-2288.

[49] P. Faucon, A. Delagrave, J.C. Petit, C. Richet, J.M. Marchand, H. Zanni, Aluminum incorporation in calcium silicate hydrates (C-S-H) depending on their Ca/Si ratio, J Phys Chem B, 103 (1999) 7796-7802.

[50] S.-D. Wang, K.L. Scrivener, ^{29}Si and ^{27}Al NMR study of alkali-activated slag, Cem Concr Res, 33 (2003) 769-774.

[51] P.J. Schilling, L.G. Butler, A. Roy, H.C. Eaton, ^{29}Si and ^{27}Al MAS-NMR of NaOH-activated blast-furnace slag, J Am Ceram Soc, 77 (1994) 2363-2368.

[52] T.-J. Park, S.-S. Choi, Y. Kim, ^{27}Al solid-state NMR structural studies of hydrotalcite compounds calcined at different temperatures, Bull Korean Chem Soc, 30 (2009) 149-152.

[53] K.J.D. MacKenzie, R.H. Meinhold, S. B.L., Z. Xu, ^{27}Al and ^{25}Mg solid-state magic-angle spinning nuclear magnetic resonance study of hydrotalcite and its thermal decomposition sequence, J Mater Chem, 3 (1993) 1263-1269.

[54] P.J. Sideris, F. Blanc, Z. Gan, C.P. Grey, Identification of cations clustering in Mg-Al layered double hydroxides using multinuclear solid state nuclear magnetic resonance spectroscopy, Chem Mater, 24 (2012) 2449-2461.

[55] P. Pena, J.M. Rivas Mercury, A.H. de Aza, X. Turrillas, I. Sobrados, J. Sanz, Solid-state ^{27}Al and ^{29}Si NMR characterization of hydrates formed in calcium aluminate-silica fume mixtures, J Solid State Chem, 181 (2008) 1744-1752.

[56] J.M. Rivas Mercury, P. Pena, A.H. De Aza, X. Turrillas, I. Sobrados, J. Sanz, Solid-state ^{27}Al and ^{29}Si NMR investigations on Si-substituted hydrogarnets, Acta Mater, 55 (2007) 1183-1191.

[57] S. Martínez-Ramírez, M. Frías, The effect of curing temperature on white cement hydration, Constr Build Mater, 23 (2009) 1344-1348.

[58] M.D. Andersen, H.J. Jakobsen, J. Skibsted, Incorporation of aluminum in the calcium silicate hydrate (C-S-H) of hydrated Portland cements: A high-field ^{27}Al and ^{29}Si MAS NMR Investigation, Inorg Chem, 42 (2003) 2280-2287.

[59] M.D. Andersen, H.J. Jakobsen, J. Skibsted, A new aluminium-hydrate species in hydrated Portland cements characterized by ^{27}Al and ^{29}Si MAS NMR spectroscopy, Cem Concr Res, 36 (2006) 3-17.

[60] J.R. Barnes, A.D.H. Clague, N.J. Clayden, C.M. Dobson, C.J. Hayes, G.W. Groves, S.A. Rodger, Hydration of Portland cement followed ^{29}Si solid-state NMR spectroscopy, J Mater Sci Lett, 4 (1985) 1293-1295.

[61] G. Engelhardt, D. Michel, High-Resolution Solid-State NMR of Silicates and Zeolites, John Wiley & Sons, Chichester, 1987.

[62] R.J. Kirkpatrick, MAS NMR-Spectroscopy of minerals and glasses, Rev Mineral, 18 (1988) 341-403.

[63] G. Le Saoût, M. Ben Haha, F. Winnefeld, B. Lothenbach, Hydration degree of alkali-activated slags: A ^{29}Si NMR study, J Am Ceram Soc, 94 (2011) 4541-4547.

[64] P. Rejmak, J.S. Dolado, M.J. Stott, A. Ayudala, ^{29}Si NMR in cement: A theoretical study on calcium silicate hydrates, J Phys Chem C, 116 (2012) 9755-9761.

[65] R.J. Myers, S.A. Bernal, R. San Nicolas, J.L. Provis, Generalized structural description of calcium-sodium aluminosilicate hydrate gels: The crosslinked substituted tobermorite model, Langmuir, (2013) in press, DOI 10.1021/la4000473.

[66] A.R. Brough, A. Atkinson, Sodium silicate-based, alkali-activated slag mortars - Part I. Strength, hydration and microstructure, Cem Concr Res 32 (2002) 865-879.

[67] F. Puertas, A. Gil-Maroto, M. Palacios, T. Amat, Alkali-activated slag mortars reinforced with AR glassfibre. Performance and properties, Mater Constr, 56 (2006) 79-90.

[68] I.G. Richardson, The nature of C-S-H in hardened cements, Cem Concr Res, 29 (1999) 1131-1147.

[69] J.L. Provis, P. Duxson, G.C. Lukey, J.S.J. van Deventer, Statistical thermodynamic model for Si/Al ordering in amorphous aluminosilicates, Chem Mater, 17 (2005) 2976-2986.

[70] G. Kowalczyk, J.E. Roberts, Solid state ^{29}Si NMR determination of crystalline silica in natural iron oxide pigments, Analyt Chim Acta, 286 (1994) 25-35.

[71] S.A. Myers, R.T. Cygan, R.A. Assink, M.B. Boslough, ^{29}Si MAS NMR relaxation study of shocked Coconino Sandstone from Meteor Crater, Arizona, Phys Chem Miner, 25 (1998) 313-317.

[72] H. He, J. Guo, J. Zhu, P. Yuan, C. Hu, ^{29}Si and ^{27}Al MAS NMR spectra of mullites from different kaolinites, Spectrochim Acta A, 60 (2004) 1061-1064.

[73] L.H. Merwin, A. Sebald, H. Rager, H. Schneider, ^{29}Si and ^{27}Al MAS NMR spectroscopy of mullite, Phys Chem Miner 18 (1991) 47-52.

[74] A. Palomo, S. Alonso, A. Fernández-Jiménez, I. Sobrados, J. Sanz, Alkaline activation of fly ashes: NMR study of the reaction products, J Am Ceram Soc, 87 (2004) 1141-1145.

[75] P. Duxson, G.C. Lukey, F. Separovic, J.S.J. van Deventer, The effect of alkali cations on aluminum incorporation in geopolymeric gels, Ind Eng Chem Res, 44 (2005) 832-839.

[76] J.J. Chen, J.J. Thomas, H.M. Jennings, Decalcification shrinkage of cement paste, Cem Concr Res, 36 (2006) 801-809.

[77] J.L. Provis, A. Hajimohammadi, C.E. White, S.A. Bernal, R.J. Myers, R.P. Winarski, V. Rose, T.E. Proffen, A. Llobet, J.S.J. van Deventer, Nanostructural characterization of geopolymers by advanced beamline techniques, Cem Concr Compos, 36 (2013) 56-64.